Nitrogen-doped porous carbon nanofibers embedded with Cu/Cu_3P heterostructures as multifunctional current collectors for stabilizing lithium anodes in lithium-sulfur batteries

Xiang, Yinyu; Lu, Liqiang; Li, Wenjian; Yan, Feng; Wang, Hui; Zhao, Zelin; Li, Junsheng; Giri Prakash Kottapalli, Ajay; Pei, Yutao

Published in:
Chemical Engineering Journal

DOI:
10.1016/j.cej.2023.145089

Publication date:
2023

Chemical Engineering Journal 472 (2023) 145089

Contents lists available at ScienceDirect

Chemical Engineering Journal

journal homepage: www.elsevier.com/locate/cej

Nitrogen-doped porous carbon nanofibers embedded with Cu/Cu_3P heterostructures as multifunctional current collectors for stabilizing lithium anodes in lithium-sulfur batteries

Yinyu Xiang [a], Liqiang Lu [a], Wenjian Li [a], Feng Yan [b], Hui Wang [c], Zelin Zhao [d], Junsheng Li [d], Ajay Giri Prakash Kottapalli [a], Yutao Pei [a,*]

[a] Advanced Production Engineering, Engineering and Technology Institute Groningen, University of Groningen, 9747AG Groningen, the Netherlands
[b] National Graphene Institute, University of Manchester, Manchester M13 9PL, UK
[c] Nanostructured Materials and Interfaces, Zernike Institute for Advanced Materials, University of Groningen, 9747AG Groningen, the Netherlands
[d] School of Chemistry, Chemical Engineering and Life Sciences, Wuhan University of Technology, 430070 Wuhan, PR China

ARTICLE INFO

Keywords:
Cu/Cu_3P heterostructures
Li deposition
Lithium dendrite
Current collector
Li-S batteries

ABSTRACT

Among the various beyond-lithium-ion battery systems, lithium-sulfur batteries (Li-S) have been widely considered as one of the most promising technologies owing to their high theoretical energy density. However, the irregular Li plating/stripping and infinite volume change associated with low Coulombic efficiency and safety concerns of host-less lithium anode hinder the practical application of Li-S batteries. Herein, Cu/Cu_3P heterostructure-embedded in carbon nanofibers (Cu/Cu_3P-N-CNFs) are developed as multifunctional current collectors for regular lithium deposition. The 3D porous interconnected carbon skeleton endows effectively reduced local current density and volume expansion, meanwhile the Cu/Cu_3P particles function as nucleation sites for uniform lithium plating. Consequently, the developed ion/electron-conducting skeleton delivers remarkable electrochemical performances in terms of high Coulombic efficiency for 500 cycles at 1 mA cm^{-2}, and the accordingly symmetric cell exhibits long-term cyclic duration over 1500 h with a low voltage hysteresis of ~ 80 mV at 1 mA cm^{-2}. Moreover, Li-S full cells paired with the developed anode and S@CNTs cathode also show superior rate capability (568 mAh/g at 2C) and excellent stability of >500 cycles at 0.2C, further demonstrating the great potential of Cu/Cu_3P-N-CNFs as promising current collectors for advanced lithium-metal batteries.

1. Introduction

Amongst the most promising next-generation energy storage devices, lithium-sulfur (Li-S) batteries with ultrahigh specific theoretical energy density (2600 Wh kg^{-1}) have marked a unique position due to the high theoretical capacities of both the sulfur cathode (1675 mAh/g) and lithium anode (3800 mAh/g) [1,2]. Nevertheless, some main challenges, including notorious polysulfide shuttling originating from sulfur cathode and uncontrollable dendritic growth of lithium on anodes, still need to be addressed before the commercialization of Li-S batteries [3,4].

Extensive efforts including rational design of sulfur hosts [5–8], introduction of functional interlayers/coating layers [9–12], design of polysulfide electrocatalysis [13], optimization of electrolytes with additives [14,15], and novel binders [16,17] have been explored to circumvent inferior conductivity of sulfur cathodes, dissolution of polysulfides, and irreversible deposition of Li_2S. Despite the significant achievements towards improving the performance of sulfur cathodes, the obstacles such as dendritic growth, fragile solid electrolyte interface (SEI), and large volume change associated with metallic Li anode still impede the practical application of Li-S batteries [18–20]. To solve the challenging issues of Li dendrites, several approaches including modification of electrolytes and utilization of high-modulus artificial SEI [21,22], sol–gel electrolyte [23] or solid-state electrolyte [24–26] have been adopted to suppress the dendrite penetration. Nevertheless, as host-less metallic lithium has been configured in these works, infinite volume expansion still remains a bottleneck during battery operation. Moreover, mostly excessive metallic lithium (~50 μm for pouch cells and ~ 0.5 mm for coin cells) used in laboratories is a serious waste of

* Corresponding author.
E-mail address: y.pei@rug.nl (Y. Pei).

https://doi.org/10.1016/j.cej.2023.145089
Received 28 April 2023; Received in revised form 21 July 2023; Accepted 27 July 2023
Available online 29 July 2023

anode capacity, inevitably raising the cost of batteries due to the high and increasing price of lithium.

In this regard, constructing 3D electronically conductive current collectors for uniform Li deposition is highly desired for stable anodes that match the capacity of cathodes in Li-S batteries [27]. In particular, a variety of 3D carbon frameworks, including 3D porous graphene [28], 3D hollow carbon fibers [29], and hierarchical porous carbon materials [30] have been reported to inhibit the Li dendrites. First, the 3D nanostructured host can effectively decentralize the surface current density distribution and play a role in homogenizing electric field, improving the uniformity during Li (or other metals) deposition [31,32]. Furthermore, carbon frameworks are more stable, lighter and cheaper than metallic current collectors to accommodate the large volume variation during Li growth. To further guide the uniform Li nucleation, lithiophilic sites, such as polar functional heteroatom-dopants (e.g. nitrogen [33], oxygen [34,35]) or metal particles (e.g. Zn [36], Ag [37,38], and Co/Ni [39]), or metallic compounds (oxides [40], sulfides [41], and phosphides[42]) are introduced into carbon skeletons. For instance, lithiophilic chemistry of various dopants was probed to guide uniform heterogeneous Li nucleation through both first-principle simulations and experimental verifications [43]. Yan et al. investigated the Li deposition behavior on nanoparticles-embedded hollow carbon spheres, and confirmed that Li metal could be selectively deposited onto Zn, Ag, and Au nanoseeds owing to low lattice misfits between these metals and Li and the formation of alloys with Li, contributing to ultralow or zero nucleation overpotentials [44]. In addition, the uniform electrostatic potential field and the low lattice misfits between Li host and metallic Li are also significant for achieving zero or ultralow-overpotential nucleation, which could also be expanded to other metal electrodepositions, such as in magnesium-metal batteries [45,46]. Recently, cobalt phosphide-modified carbon nanofibers were proposed to suppress the lithium dendrites by uniform nucleation because of the reaction between lithiophilic metallic phosphides and Li, as well as the high Li^+ conductivity of discharge product (Li_3P) [47]. Whereas, metallic phosphide particles have inferior electronic conductivity than metal particles, which can negatively affect the transport of electrons during the lithium nucleation and further growth [48]. During the past decade, metal/compound heterostructures (e.g. Ag-Cu_3P [49], Ag-TiO_2 [50], Au-TiO_2 [51] and dealloyed Cu/CuSe [52]) that simultaneously possess high electronic conductivity and superior Li^+ conductivity showed great potential in energy storage and conversion. Particularly, dealloyed Cu/CuSe integrated the high electronic conductivity of Cu substrate and the high lithiophilicity of CuSe granules, contributing to the regulated Li plating/stripping and stabilized Li@Cu/CuSe anodes [52]. However, a facile and sustainable strategy to obtain lithiophilic current collectors with both superior ionic and electronic conductivity for effective Li storage is still in an urgent need. More important, the thin and light host plays a significant role in maintaining high energy density of batteries (both volumetric and gravimetric), which should be fully considered before the commercialization.

In this work, we present the elaborate design and large-area fabrication of a 3D current collector consisting of nitrogen-doped porous carbon fibers featuring abundant copper-based Cu/Cu_3P heterostructure decorations (Cu/Cu_3P-N-CNFs) for stable Li metal anodes. The Li plating/stripping can be effectively regulated with the Cu/Cu_3P-N-CNFs host owing to the following multifold merits: (1) effectively decreased local current density due to the large surface area of 3D porous conductive frameworks, (2) stable and interconnected porous structure to buffer the volume variation, (3) lithiophilic nitrogen dopants to homogenize Li deposition, (4) mixed electron/ion-conducting Cu/Cu_3P to eliminate the barriers for Li nucleation owing to the formation of Li_3P and enhanced electron transport through the copper heterostructure. Benefiting from the above advantages, uniform and even Li plating on Cu/Cu_3P-N-CNFs host is realized. The structural and compositional merits endow Cu/Cu_3P-N-CNFs electrodes with a regular plating/stripping behavior for >500 cycles at 1 mA cm^{-2} with the capacity of 1 mAh cm^{-2}. Additionally, the developed Li@Cu/Cu_3P-N-CNFs anodes (loaded with 5 mAh cm^{-2} Li) deliver excellent stability up to 1500 h in symmetrical cells tests at 1 mA cm^{-2} for 1 mAh cm^{-2} Li plating/stripping. More importantly, long lifespan and fantastic electrochemical performance are achieved for Li-S full cells equipped with Li@Cu/Cu_3P-N-CNFs anodes under a low anode/cathode capacity ratio of ~ 2:1 and a high sulfur loading (4.1 mg cm^{-2}) condition.

2. Experimental section

2.1. Sample preparations

Preparation of Cu/Cu_3P heterostructure-embedded carbon nanofibers (Cu/Cu_3P-N-CNFs): 1.3 g polyacrylonitrile (PAN, Mw = 150000, Aldrich) and 0.2 g urea were dissolved in 10 g N, N-dimethylformamide (DMF, 99.8%, Aldrich) by vigorous stirring at 70 °C for overnight and the mixture was named as solution A. Solution B: 0.15 g P_2O_5 and 0.25 g $CuCl_2$ (98%, Alfa Aesar) were dissolved in 3 g DMF by magnetic stirring. Then, solution B was mixed with solution A by magnetic stirring for another 2 h. P_2O_5-$CuCl_2$-urea@PAN fibers were obtained by electrospinning with the above mixture solution using a NanoSpinner NE300 machine. The electrospinning parameters including the voltage, feeding rate, distance between the collector and the needle, diameter of the needle, and spin time were fixed at 16 kV, 0.8 mL h^{-1}, 15 cm, 1.2 mm, and 7 h, respectively. Thereafter, the as-collected P_2O_5-$CuCl_2$-urea@PAN fibers were heated at 300 °C for 2 h, and then calcined at 800 °C for another 2 h in vacuum with the heating rate of 5 °C min^{-1}. For the sake of comparison and optimization, Cu/Cu_3P-N-CNFs-1 and Cu/Cu_3P-N-CNFs-2 were also prepared with the introduction of 0.1 g and 0.2 g P_2O_5, respectively. Cu_3P-embedded carbon nanofibers (Cu_3P-N-CNFs) were prepared using the similar procedure to the one used for preparing Cu/Cu_3P-N-CNFs except for the fact that more P_2O_5 (0.3 g) was added into the mixture during electrospinning, while the Cu-embedded carbon nanofibers (Cu-N-CNFs) were also synthesized without adding P_2O_5.

Preparation of sulfur@carbon nanotubes composite (S@CNTs): Sulfur (0.21 g) and carbon CNTs (0.09 g) were added into 10 mL carbon disulfide/N-methyl-2-pyrrolidone (7:3 v/v) followed by magnetic stirring at 70 °C overnight. After the solvent was fully evaporated, the mixture was heated at 155 °C for 20 h under argon atmosphere.

2.2. Characterizations

The morphologies and structures of fiber samples were characterized by scanning electron microscope (SEM, FEI Nova NanoSEM 650 and TESCAN Lyra) and transmission electron microscope (TEM, JEOL JEM-2200FS) equipped with an energy dispersive spectroscopy (EDS) detector. X-ray diffraction (XRD) patterns were collected from D8 Advance diffractometer with a Cu Kα source (λ = 1.54 Å) to examine the crystallinity of samples. The refinement for Cu/Cu_3P-N-CNFs sample was conducted to estimate the content of Cu_3P phase using Maud software [53]. To confirm sulfur content of S@CNTs, thermogravimetric analysis (TGA) was conducted on a Perkin Elmer TGA 4000 system in a temperature ranging from room temperature to 700 ℃ at a heating rate of 10 ℃ min^{-1} in N_2 atmosphere. The Cu and Cu_3P content in nanofibers composites were examined using TGA from room temperature to 700 °C with a heating rate of 10 ℃ min^{-1} under air atmosphere. Raman spectrums were measured in an optical cryostat (ST500, Janis) excited at 532 nm (Cobalt Samba^T *M* 25). The nitrogen adsorption–desorption isotherms were recorded to analyze the porosities of samples using a Micromeritics ASAP 2420 porosimeter at −196 °C. The Li plating and stripping morphologies on current collators were also characterized by SEM. The discharged/charged half-cells were disassembled in the Ar-filled glovebox and the working electrodes that deposited/stripped with different amount lithium were stored in the Ar-filled centrifuge tubes, and then quickly transferred into the SEM chamber. To characterize the chemical states of electrodes, X-ray photoelectron

spectroscopy (XPS) measurements were conducted with the Surface Science Instruments SSX-100 spectrometer, equipped with a monochromatic Al $K\alpha$ X-ray source (hv = 1486.6 eV). For fresh electrodes, the circular disks with the diameter of 12 mm were fixed on the stainless-steel holder and transferred into the chamber of equipment without protection. For the discharged electrodes, the transfer was conducted quickly with Ar protection. The pressure of the measurement camper was kept at 1×10^{-9} mbar during data collection. The photoelectron take-off angle was 37° with respect to normal surface. The energy resolution was 1.26 and 1.67 eV for high-resolution test and wide scan, respectively. Spectral analysis including a Shirley background subtract and fitting with peak profiles was taken as convolution of Gaussian and Lorentzian functions, according to the last squares curve-fitting program WinSpec (LISE, University of Namur, Belgium). All binding energies were referred to C 1s photoemission peak (284.8 eV) and the accuracy was ± 0.1 eV when deducing the fitting procedure. To estimate the electrical conductivity of carbon films, stainless steel || stainless steel coin cells were assembled, wherein the carbon films were sandwiched between the stainless steels. Then the electrical resistance of the cells was measured using a multimeter (Keithley). Since the stainless-steel plate is thin and highly conductive, the resistance of the carbon film was approximately considered to be the resistance of the coin cell.

2.3. Electrochemical measurements

The electrolyte used was 1 M lithium bis(trifluoromethanesulfonyl) imide (LiTFSI) in 1:1 (v/v) 1,2-dimethoxyethane (DME) and 1,3-dioxacyclopentane (DOL) with 3% $LiNO_3$ as additive, and the separator was Celgard 2400. The electrochemical impendence spectrums (EIS) were collected using CHI 760E electrochemical working station (Shanghai, China), and the battery performance was recorded using a LAND (Wuhan, China) battery tester.

Li || Cu and Li || N-CNFs half-cells for evaluating Coulombic efficiency of lithium plating/striping were assembled in the Ar-filled glovebox using Li foils as both reference and counter electrodes, copper foils, Cu-N-CNFs, Cu_3P-N-CNFs or Cu/Cu_3P-N-CNFs as working electrode, and the amount of electrolyte for each cell was controlled at 40 μL. To form a relatively stable SEI on the Li hosts, the batteries were first cycled between 0.01 V and 1.5 V (versus Li/Li^+) at 0.1 mA cm^{-2} for the initial three cycles. For lithium plating, the capacity was 1 mAh cm^{-2} (at 1 mA cm^{-2}), and the cut-off voltage for lithium stripping was 1.5 V.

Li || Li symmetric cells: 5 mAh cm^{-2} of Li was plated onto the planar Cu foil, Cu-N-CNFs, Cu_3P-N-CNFs, or Cu/Cu_3P-N-CNFs at a current density of 1 mA cm^{-2} to form the Li@Cu foil, Li@Cu-N-CNFs, Li@Cu_3P-N-CNFs and Li@Cu/Cu_3P-N-CNFs electrodes. Symmetric cells containing the same electrodes for working and counter electrodes were assembled using Li@Cu foil, Li@Cu-N-CNFs, Li@Cu_3P-N-CNFs and Li@Cu/Cu_3P-N-CNFs electrodes, respectively, to measure the long-term electrochemical behavior of Li plating/stripping. The amount of electrolyte for each cell was 40 μL.

Li-S full cell: the cathode contained 80 wt% S@CNTs composite, 10 wt% Super P, and 10 wt% polyvinylidene difluoride binder using N-methyl-2-pyrrolidone as the solvent, and the well-mixed slurry was cast onto Al foil. The mass loading of sulfur was 1.2–1.4 mg cm^{-2}, and the electrolyte to sulfur mass ratio (E/S) was controlled at 15 μL, 7 μL, or 5 μL per milligram of sulfur. The anodes were Li pre-deposited with 5 mAh cm^{-2} Li onto different hosts. In addition, the Li@ Cu/Cu_3P-N-CNFs anode with Li loading of 12 mAh cm^{-2} were also paired with S@CNTs cathode with higher sulfur loading of ~ 4.1 mg cm^{-2} for Li-S full-cell assessment. The E/S in full cells was controlled at 10 μL mg^{-1}. The charge/discharge capacity was calculated based on the mass of loaded sulfur.

2.4. Simulations for electric field

The finite element simulations were conducted on COMSOL Multiphysics 5.2a. Simplified models were used to simulate the electric field for Cu/Cu_3P-N-CNFs and Cu foil. In the case of Cu/Cu_3P-N-CNFs, a 15 × 6 nanofiber array with a gap of 2000 nm along both X and Y direction was modeled as the nanofiber electrode. The diameter of the fibers was set as 500 nm according to the SEM images. Electrostatics interface in the COMSOL AC/DC module and stationary study were applied to obtain the simulation results.

2.5. Density function theory (DFT) calculation

First-principles calculations were conducted with the Vienna ab initio Simulation Package [54] based on the DFT to investigate the structure and conductivity of Cu, Cu_3P and Cu/Cu_3P. The generalized gradient approximation (GGA) with the scheme of Perdew-Burke-Ernzerhof (PBE) was employed to calculate the exchange–correlation energy. The van der Waals correction DFT-D3 was considered during the calculation. For the surface system (Cu_3P/Cu), vacuum slab in the vertical direction was set at 15 Å. The cutoff energy was set at 500 eV, and the Monkhorst-Pack k-point meshes of Cu_3P/Cu, Cu_3P and Cu were 3 × 3 × 1, 9 × 9 × 7 and 9 × 9 × 9, respectively. The structures were relaxed until the forces and total energy on all atoms were converged to less than 0.02 eV $Å^{-1}$ and 1×10^{-5} eV. The density of states (DOS) was calculated via the Gaussian smearing method setting with a smearing width of 0.05 eV.

3. Results and discussion

As schematically illustrated in Fig. 1a, the fabrication of Cu/Cu_3P-N-CNFs was realized through a facile process, which involved electrospinning followed with a carbothermic reduction pyrolysis process. During the pyrolysis process, PAN nanofibers provide the 3D frameworks, urea can enhance the nitrogen content and generate pores due to thermal decomposition, P_2O_5 serves as an oxidizing agent and the phosphorus source, and $CuCl_2$ is the precursor of copper nanoparticles and copper phosphide.

The electric field distributions in 3D framework and 2D planar models were simulated during Li plating for the evaluation of electric field distributions in Cu/Cu_3P-N-CNFs and Cu foil electrodes, respectively. As it can be compared from Fig. 1b and 1d, Cu/Cu_3P-N-CNFs host exhibits much lower electric-field intensity than Cu foil due to the reduced local current density during Li deposition on 3D porous structures. The structural advantage of Cu/Cu_3P-N-CNFs is beneficial for the regulated Li deposition (Fig. 1c) [55]. In comparison, the Li plating/stripping on Cu foil was reported to have inhomogeneous Li nucleation, uncontrollable formation of dead Li and Li dendrites due to various aspects including the inferior lithiophilicity and limited space for Li growth of planar Cu foil. (Fig. 1e) [56,57].

Fig. S1a and b show the prepared precursor film and the calcined carbon film with well-maintained integrities, respectively, indicating that the method holds great potential for large-scale synthesis. The as-prepared Cu/Cu_3P-N-CNFs film also exhibits superior flexibility and decent mechanical properties, which could be visually confirmed by various mechanical deformations (Fig. S1c–h) like bending, rolling, and folding, demonstrating the excellent ability to buffer compressive stress during battery operation. The areal density and the thickness of the carbon films are measured to be ~ 1.5 mg cm^{-2} (measured by highly accurate analytical balance) and ~ 50 μm (Fig. S1i–k) respectively, much lower and thinner than some reported carbon-based hosts (Table S2). The precursor for preparing Cu/Cu_3P-N-CNFs exhibits interlaced fabric structures and the diameter of the fibers is about 400–450 nm (Fig. S2). In addition, C, N and O elements are uniformly distributed in the nanofibers and constitute the fabric framework, while Cl, Cu and P elements are distributed on the whole film (Fig. S2). After carbonization, the diameter of Cu/Cu_3P-N-CNFs is slightly thinner (350–400 nm, Fig. 2c) than the precursor due to the shrinkage of PAN nanofibers, and Cl element is disappeared owing to the decomposition of

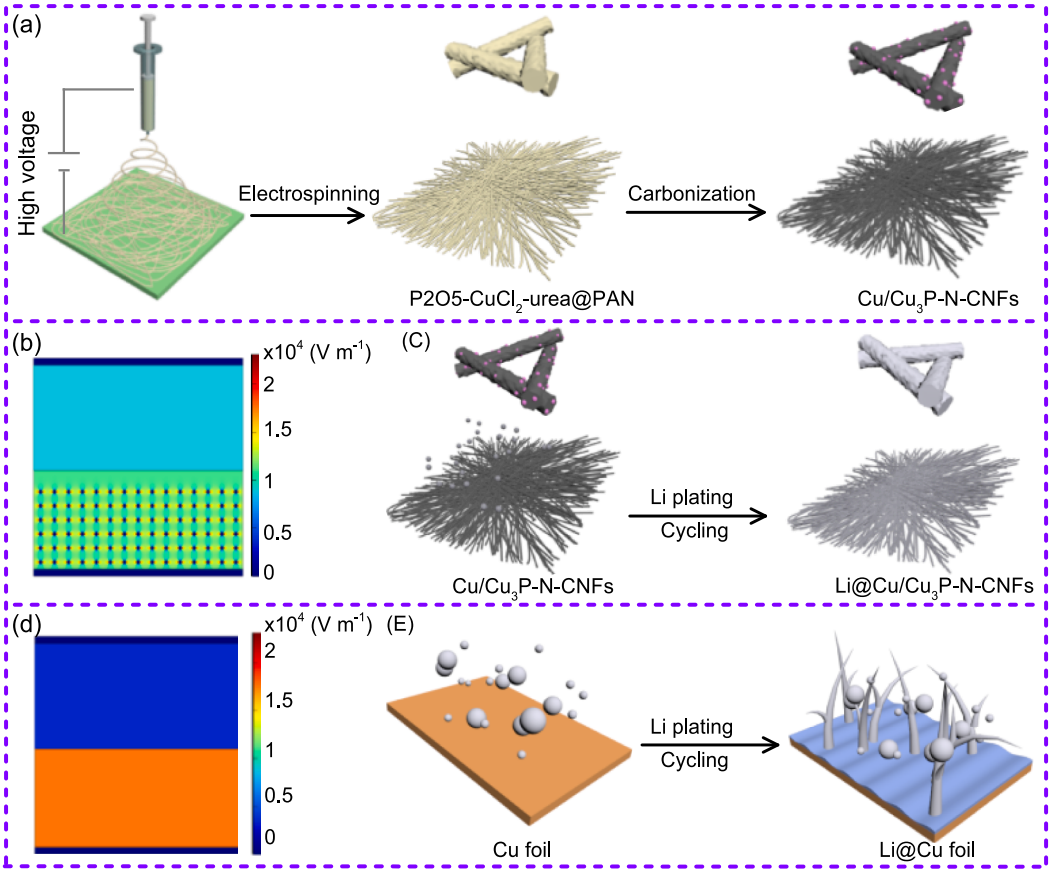

Fig. 1. (a) The schematic illustration for the synthesis of Cu/Cu_3P-N-CNFs current collectors. (b) and (d) are simulated electric field distributions for Cu foil and Cu/Cu_3P-N-CNFs in half-cell systems. Schematic illustrations for the Li deposition on Cu/Cu_3P- N-CNFs (c) and Cu foil (e).

$CuCl_2$ (Fig. S3). For comparison, Cu-N-CNFs (Fig. 2a) and Cu_3P-N-CNFs (Fig. 2b and Fig. S5) are prepared using the similar process with different P_2O_5 ratios, and the precursor exhibits the similar fabric structures (Fig. S4). As shown in the high-resolution SEM images (insets in Fig. 2a–c) and transmission electron microscopy (TEM) images (Fig. 2d–f), nanofibers embedded with some nanoparticles can be observed for all the three samples, and the size of nanoparticles ranges from tens of nanometer to about 100 nm. High-resolution TEM (HRTEM) images in Fig. 2g and h show obvious lattice fringes with a spacing of 0.209 nm and 0.249 nm, respectively, attributing to the (1 1 1) lattice plane of Cu and (1 1 2) plane of Cu_3P. By contrast, the HRTEM of Cu/Cu_3P-N-CNFs (Fig. 2i) presents distinct fringe interfaces and disordered areas. The lattice spacings of 0.183 nm and 0.209 nm correspond to the (2 0 0) and (1 1 1) planes of Cu nanoparticles, respectively. The (1 1 2) plane of Cu_3P with the lattice spacing of 0.249 nm can be also observed, confirming the formation of Cu/Cu_3P heterostructure. The corresponding fast-Fourier-transform (FFT) patterns of selected areas are presented in the insets of Fig. 2g–i. The FFT pattern of Cu-N-CNFs shows a pair of symmetrical dots and the distance between which was 9.8 1/nm, corresponding to d space of 0.208 nm for Cu (1 1 1). Both the FFT patterns of Cu_3P-N-CNFs and Cu/Cu_3P-N-CNFs show a similar ring, the diameter of which is 8.02 1/nm, corresponding to d space of 0.249 nm for Cu_3P (1 1 2). Cu/Cu_3P-N-CNFs are also characterized with EDS mapping (Fig. S6). Cu element is mainly dispersed in the particles, while P element is dispersed in both the particles and nanofibers. In addition, only the core part of the particles is mapped with P element, indicating the coexistence of Cu and Cu_3P in one particle. Compared to 3.2 % atomic content of P element, the atomic content of Cu element was much higher (12.4%) for the selected area, which further confirmed the Cu/Cu_3P heterostructure. Cu/Cu_3P heterostructure combines the high conductivity of Cu and high lithiophilicity of Cu_3P, and can sever as a mixed electron/ion conductor during lithium nucleation and growth, which is expected to regulate the lithium deposition/stripping [58].

The XRD patterns (Fig. 2j and Fig. S7a) of all three kinds of nanofibers show a broad peak at 2θ of 20-30°, which is attributed to the amorphous carbon fibers. The peaks at 2θ = 43.3°, 50.5° and 74.2° for Cu-N-CNFs and Cu/Cu_3P-N-CNFs are corresponded to 111, 200 and 220 planes of Cu (PDF #85-1326), while the peaks at 2θ = 36.1°, 39.1°, 41.4°, 45.1° and 46.3° for Cu_3P-N-CNFs and Cu/Cu_3P-N-CNFs samples confirm the presence of Cu_3P (PDF #71-2261). These results demonstrate the formation of Cu and Cu_3P nanoparticles in Cu/Cu_3P-N-CNFs. Based on the refined XRD result (Fig. S7a), the weight content of Cu phase and Cu_3P phase in Cu/Cu_3P heterostructure was estimated to be 72.5% and 27.5%, respectively. In addition, we calculated the crystallite size from the XRD peaks based on Debye-Scherrer equation. The average crystallite size of Cu/Cu_3P particle is 35.6 nm, which is consistent with the TEM observations.

Based on the analysis of N_2 adsorption–desorption, the three films show similar isotherms (IV type) with hysteresis loops at relatively high pressure of 0.5–1 (Fig. 2k), indicating the hierarchical porous structures with micropores/small mesopores (<5 nm) and large mesopores (>15 nm) (Fig. S7b). The micropores/small mesopores were generated due to the gas activation (decomposition of urea and reduction of P_2O_5) [42,59], while the large mesopores could be arisen from the stacking of nanofibers [47]. In addition, the BET surface areas of Cu-N-CNFs, Cu/Cu_3P-N-CNFs and Cu_3P-N-CNFs were calculated to be 23.3, 27.8 and 32.6 $m^2\ g^{-1}$, respectively. Raman spectra (Fig. 2l) were depicted to explore the amorphous structure of as-synthesized carbon films. Two representative peaks of the carbon films at ~ 1346 cm^{-1} and ~ 1590 cm^{-1} are assigned to the disordered structure (D-band) and graphitic sp^2 carbon (G-band), respectively. The high intensity ratios I_D/I_G further manifest the low graphitization degree of amorphous carbon fibers in

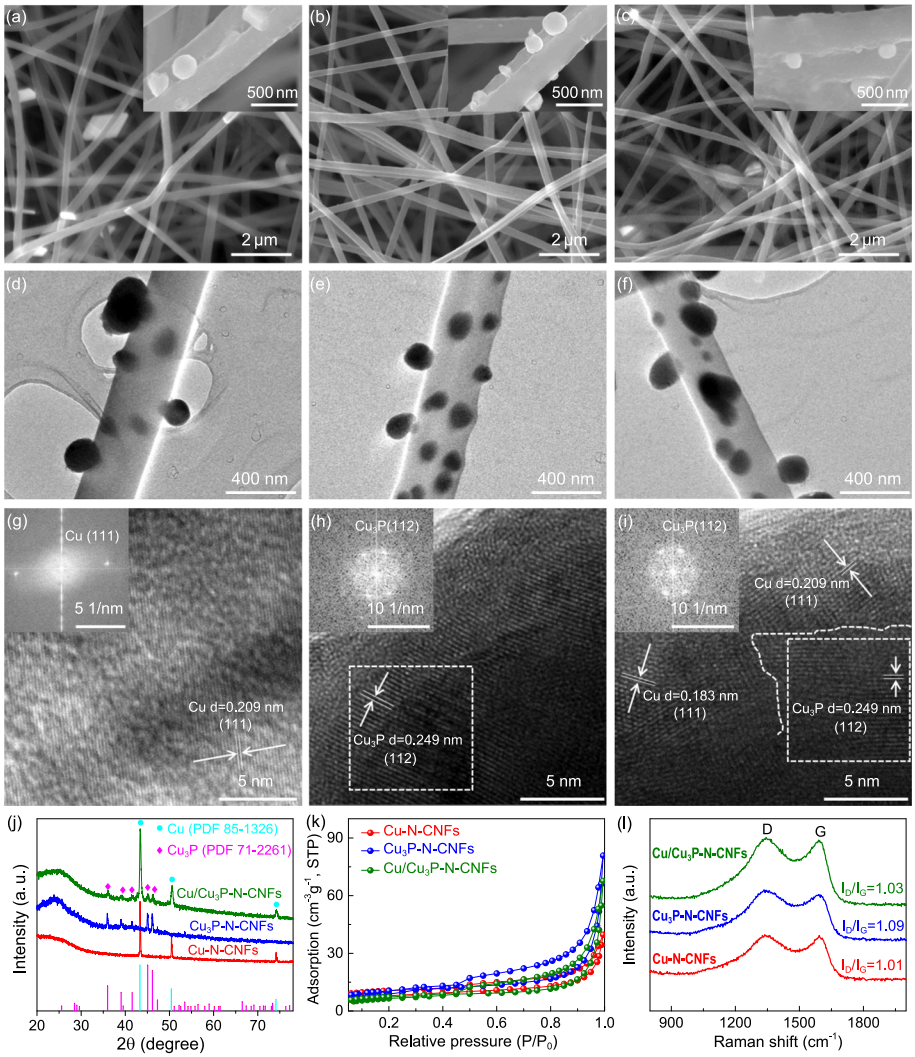

Fig. 2. Characterization of prepared 3D current collectors. SEM images of (a) Cu-N-CNFs, (b) Cu_3P-N-CNFs and (c) Cu/Cu_3P-N-CNFs. (d-f) are the corresponding TEM images. (g-i) are the corresponding HRTEM images (the insets are corresponding fast-Fourier-transfer patterns). (j) XRD patterns, (k) nitrogen adsorption/desorption isotherms and (l) Raman spectra of the three fabric hosts, respectively.

these composites. Moreover, the I_D/I_G ratio increases with the increasing phosphorization degree assuming more P_2O_5 can etch carbon skeleton and lead to more defects. To verify the content of nanoparticles in the nanofibers, TGA measurements (Fig. S6c) were implemented under air atmosphere. The remaining weight for Cu-CNTs was ~ 21%, and the Cu content was calculated to be ~ 16.8 wt% when the transformation of Cu into CuO was considered at 800 °C [60]. The remaining weight for Cu_3P-N-CNFs was ~ 28% that weighed the oxidation products of Cu_3P, CuO and P_2O_5 [61], and thus corresponded to ~ 20 wt% Cu_3P. However, the decomposition of Cu/Cu_3P heterostructure was more complicated (details can be seen in the Support information), the Cu content and Cu_3P content in Cu/Cu_3P-N-CNFs were estimated as ~ 13.1 wt% and ~ 5.0 wt %, respectively.

The micro-morphology evolution for lithium plating onto different current collectors with various areal capacities was investigated by SEM. As shown in Fig. S8b, with the plating capacity of 2 mAh cm^{-2}, the surface of Cu electrode was covered with massive uneven dendritic Li with the length of over 20 μm. With increasing the plating capacity to 6 and 8 mAh cm^{-2}, more Li dendrites were observed and they gradually grew from tens of micrometers to ~ 100 μm. Dendritic morphology with smaller Li dendrites and uneven surface were still seen after stripping 3 h and 6 h, respectively (Fig. S8f and g). After Li was fully stripped, the surface was still not smooth and covered with some residual salt from electrolyte (Fig. S8h). In the case of Cu-N-CNFs electrode host (Fig. S9), the minority of lithium tended to nucleate and grow on the surface of nanofibers, while the majority of lithium preferred to aggregate on the top surface of Cu-N-CNFs film instead of depositing inside the whole skeletons of carbon nanofibers due to the relatively low lithiophilicity of the surface. In addition, little changes of the diameter of nanofibers can be observed in the magnified insets during the Li plating/stripping, further demonstrating the inferior lithiophilicity and non-uniform Li deposition. By sharp contrast, the surface of Li@Cu/Cu_3P-N-CNFs composite film demonstrated a much smoother and denser morphology than that of Cu-N-CNFs, in which no obvious Li dendrite and no apparent Li mossy could be observed (Fig. 3b–d), confirming the well-regulated Li deposition contributed by improved lithiophilicity. With increasing Li plating capacities to 2 mAh cm^{-2}, 5 mAh cm^{-2}, and 8 mAh cm^{-2}, the diameter of nanofibers increased to 500 nm (inset of Fig. 3b), 940 nm (inset of Fig. 3c), and ~ 1.5 μm (inset of Fig. 3d), respectively, compared to that (340 nm) of the pristine nanofibers. It clearly illustrated a homogeneous and flat lithium layer formed on the Cu/Cu_3P-N-CNFs nanofibers. Consistently, the diameter of the nanofibers was decreasing gradually during stripping (Fig. 3e–g). In particular, the surface of nanofibers became smooth after Li was fully stripped (Fig. 3g), indicating the excellent electrochemical reversibility of Cu/Cu_3P-N-CNFs nanofibers. For comparison, the Li deposition behavior on Cu_3P-N-CNFs

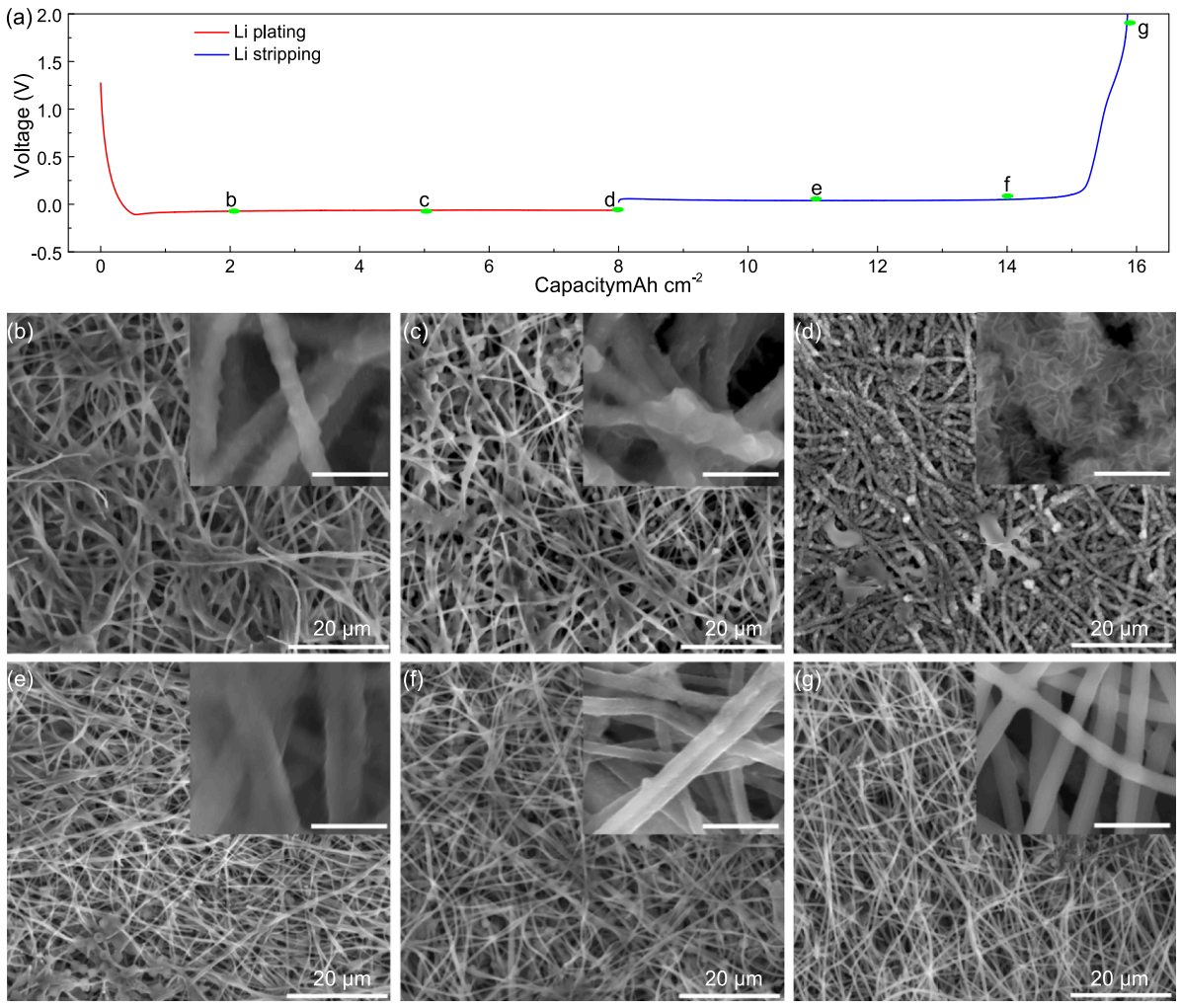

Fig. 3. (a) Electrochemical Li plating/stripping voltage profiles of Cu/Cu_3P-N-CNFs electrode with a capacity up to 8 mAh cm^{-2} at 1 mA cm^{-2}. SEM image showing Cu/Cu_3P-N-CNFs anodes after plating (b) 2 mAh cm^{-2}, (c) 5 mAh cm^{-2}, and (d) 8 mAh cm^{-2} of Li metal; SEM image revealing Li@Cu/Cu_3P-N-CNFs anodes after stripping (e) 3 mAh cm^{-2}, (f) 6 mAh cm^{-2}, and (g) 8 mAh cm^{-2} of Li. (The insets are SEM images of the nanofibers at a higher magnification. Scale bars: 2 μm).

was also recorded and shown in Fig. S10. Li tended to nucleate on the surface of lithiophilic nanofibers, leading to increased diameter during deposition and decreased diameter during stripping for nanofibers (the insets in Fig. S10). Despite the enhanced lithiophilicity of Cu_3P-N-CNFs, the Li deposition on the whole carbon film was not as even as on Cu/Cu_3P-N-CNFs. Aggregations and uneven deposition of Li could still be observed on the surface of Cu_3P-N-CNFs. The reason of this phenomenon was attributed to the inferior electric conductivity for both Cu_3P and defective carbon nanofibers, which was unfavorable for charge transfer and subsequently the Li nucleation and growth. The homogeneous lithium deposition proved the high efficiency of introducing electric/ionic conductive Cu/Cu_3P heterostructures for effective Li nucleation, and subsequent uniform construction of dendrite-free Li@Cu/Cu_3P-N-CNFs anode.

DFT calculations were conducted to gain an insight into the structures. The structures of Cu/Cu_3P, Cu_3P and Cu were optimized and depicted in Fig. S11a–f. The electronic structure calculations by density of states (DOS) bound up with the Fermi levels (Fig. S11g) were simulated to explore the total and orbital-resolved partial DOS of Cu, Cu_3P and Cu/Cu_3P. The band structure of Cu_3P rendered as a semiconductor with a band-gap near the Fermi level. However, metallicities of the hetero-structured Cu/Cu_3P were observed with the distinct and continuous Fermi levels across the conduction bands. More impressively, the DOS of Cu/Cu_3P around the Fermi level was much denser than that of Cu_3P, demonstrating the effective improvement of electronic conductivity and foreboding the enhancement of electrochemical performance.

Metallic Li plating/stripping behaviors on Cu foil, Cu-N-CNFs, Cu_3P-N-CNFs and Cu/Cu_3P-N-CNFs were further studied in half cells, in which Li foil was used as both counter and reference electrode. The Li nucleation overpotential was defined as the voltage difference between the bottom of the voltage dip and the later mass-transfer plateau [44], which is greatly depended on the affinity as well as the charge distribution of the current collectors [62]. The Li nucleation on Cu foil delivered a large overpotential of ~ 169 mV (Fig. 4a), which was used to overcome the heterogeneous nucleation barrier due to the large thermodynamic mismatch between Li and Cu [44]. In addition, the profile was not smooth and there was a sudden dip after plating for 7 h at 1 mA cm^{-2}, which could be attributed to the gradual growth of lithium dendrites (Fig. S8) [27]. By contrast, the deposition process on fabric current collectors was smoother as the 3D carbon skeletons provided much higher specific surface than 2D copper plate to reduce the local current density, and larger interconnected pores to accommodate the deposited Li. The overpotentials for Li nucleation on Cu-N-CNFs, Cu_3P-N-CNFs, and Cu/Cu_3P-N-CNFs were ~ 92 mV, ~71 mV and ~ 43 mV, respectively. Because of the formation of highly ion-conductive Li_3P during initial lithiation for Cu_3P-N-CNFs and Cu/Cu_3P-N-CNFs, these two electrodes exhibited smaller overpotentials than Cu-N-CNFs. Moreover, the Cu/Cu_3P heterostructure nanoparticles possessed higher electrical-conductivity than semi-conductive Cu_3P nanoparticles, leading to

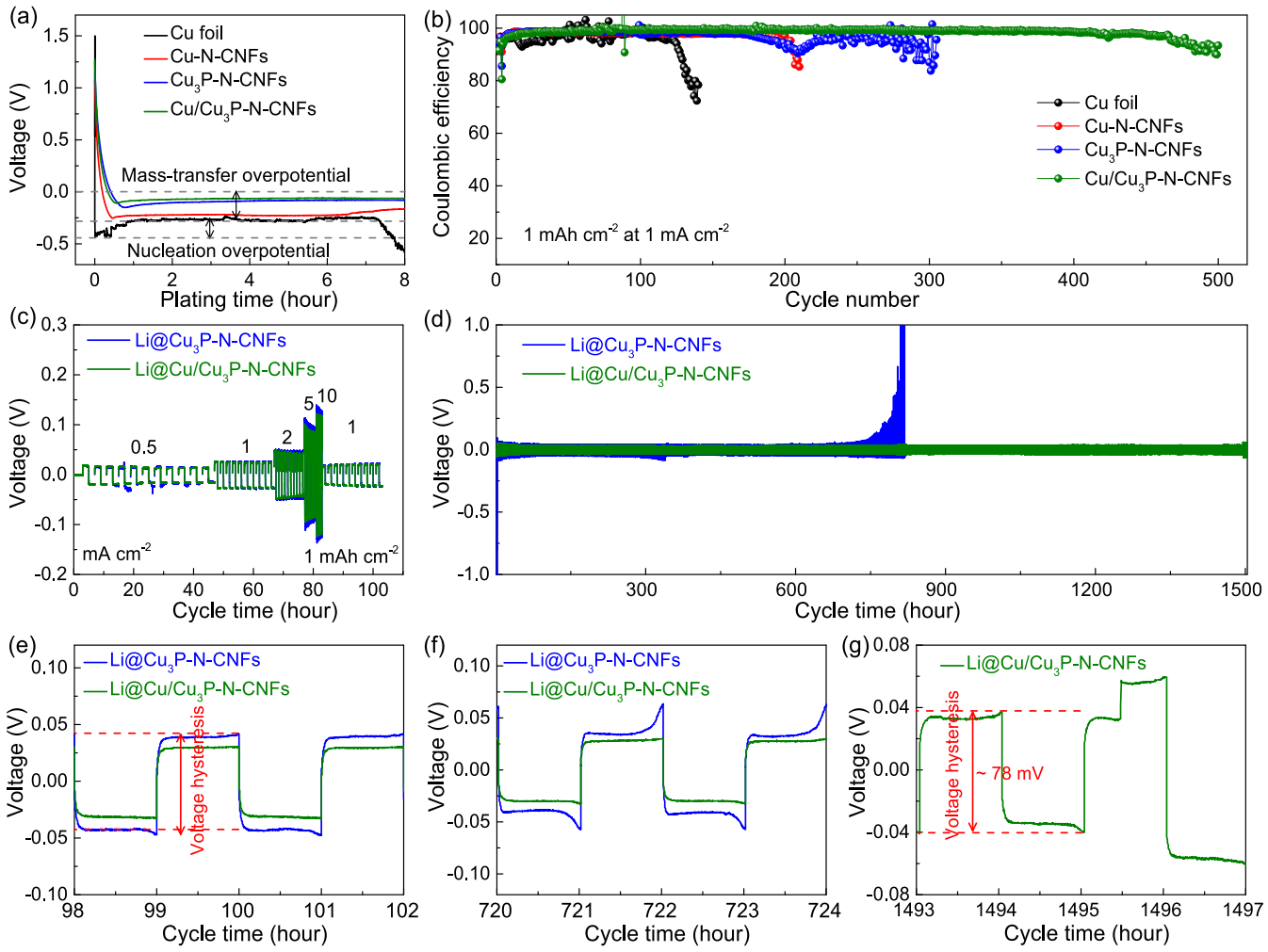

Fig. 4. Li deposition/stripping behaviors for different electrodes. (a) The voltage–time profiles for Li deposition on Cu foil, Cu-N-CNFs, Cu_3P-N-CNFs, and Cu/Cu_3P-N-CNFs current collectors at 1 mA cm^{-2}. (b) Columbic efficiency of Li stripping/deposition on different Li current collectors with the fixed capacity of 1 mAh cm^{-2}. (c) Rate performances for Li@Cu_3P-N-CNFs and Li@Cu/Cu_3P-N-CNFs in symmetric cells at different current densities with the capacity of 1 mAh cm^{-2}. (d) Long-term cyclic stability tests of Li@Cu_3P-N-CNFs and Li@Cu/Cu_3P-N-CNFs in symmetric cells at 1 mA cm^{-2} with the capacity of 1 mAh cm^{-2}. The lithium loading in Fig. c and d is 5 mAh cm^{-2}. (e-g) Enlarged profiles of selected cycles.

faster charge transfer and lower energy barrier for nucleation and mass transfer during lithiation. The electric conductivity and the EIS of the nanofibers tested with half-cells were compared in Fig. S15a and b, respectively. The lowest electric conductivity and the highest resistance of charge transfer for Cu_3P-N-CNFs further confirmed the relatively larger energy barrier and inferior electrochemical performance than Cu/Cu_3P-N-CNFs. Except the Cu/Cu_3P-N-CNFs sample with the introduction of 0.15 g P_2O_5 in the preparation system, Cu/Cu_3P-N-CNFs with the introduction of 0.1 g and 0.2 g P_2O_5 were also prepared, which were donated as Cu/Cu_3P-N-CNFs-1, and Cu/Cu_3P-N-CNFs-2, respectively. The voltage-capacity profiles for the Li deposition on Cu/Cu_3P-N-CNFs-1and Cu/Cu_3P-N-CNFs-2 were presented in Fig. S12. Despite that the nucleation overpotentials of Li deposition on Cu/Cu_3P-N-CNFs-1 (49 mV) and Cu/Cu_3P-N-CNFs-2 (43 mV) were low, which were slight larger than or equal to that on Cu/Cu_3P-N-CNFs (43 mV). However, the overpotentials for the mass-transfer process (84 mV for Cu/Cu_3P-N-CNFs-1 and 97 mV for Cu/Cu_3P-N-CNFs-2) were much higher than that on Cu/Cu_3P-N-CNFs (65 mV), which could lead to the large energy barrier for the subsequent Li growth. Thus, the Cu/Cu_3P-N-CNFs electrode with both low nucleation overpotential and low mass-transfer overpotential was selected and emphasized in our following electrochemical explorations (e. g. long-term cycling tests for half-cells, symmetrical cells and Li-S full cells).

To investigate the invertibility of Li deposition/stripping, Coulombic efficiency (CE, defined as the ratio of stripped capacity to plated capacity for each cycle) was collected (Fig. 4b). To form relatively stable SEI on current collectors, prior to cyclic tests the half cells were first activated for 3 cycles at 0.1 mA cm^{-2} from 0.01 V to 1.5 V. Li could deposit/stripe on Cu foil for 130 cycles at the current density of 1 mA cm^{-2} with the average CE higher than 85%. Then the CE rapidly declined after 130 cycles, owing to Li dendritic growth and repetitive SEI formation/destruction involving the electrolyte consumption. Due to the improved specific surface area and larger pores for accommodating Li, the Cu-N-CNFs electrodes demonstrated about 210 cycles' Li deposition/stripping. Li||Cu_3P-N-CNFs cells maintained a high CE (>90%) up to 300 cycles. However, the slight fluctuations of CE after 270 cycle may be due to the slow transfer of electrons and fewer loss of reversible Li after long-time cycling [63]. As expected, the Cu/Cu_3P-N-CNFs electrode exhibited the most stable cycling stability and longest life. Specifically, a high CE (94%) was achieved after 500 cycles for the Cu/Cu_3P-N-CNFs host, which was comparable or superior compared with the reported 3D representative Li hosts (Table S2). In addition, the charge–discharge profile of Cu/Cu_3P-N-CNFs for the first activated 3 cycles were added in Fig. S14a. In the first discharge profiles, two potential plateaus at ~ 1.7 V and ~ 0.9 V were observed. The first plateau at ~ 1.7 V was corresponded to the decomposition of $LiNO_3$ [64]. The

second plateau was corresponded to the reduction of Cu_3P during discharge, indicating the existence of conversion reaction and formation of Li_3P [58], which was also confirmed by the subsequent XPS measurements (Fig. 5b and e). However, in the subsequent charge–discharge profile, no obvious plateau was detected and confirmed that the conversion reaction was irreversible at the potential window of 0.01–1.5 V. This much-enhanced cyclic performance was consistent with the smallest overpotential of Cu/Cu_3P-N-CNFs for mass transfer and nucleation during Li plating, promoting the uniform Li^+ migration and stable cycling.

XPS measurements were conducted to detect the chemical state of current collectors. Full XPS spectrum of Cu-N-CNFs (Fig. 5a) showed six peaks at ~ 76 eV, ~285 eV, ~399 eV, ~531 eV, ~933 eV and ~953 eV, which were attributed to Cu 3p, C 1s, N 1s, O 1s, Cu $2p_{3/2}$ and Cu $2p_{1/2}$, respectively. Compared with Cu-N-CNFs, an additional P 2p signal was observed for Cu_3P-N-CNFs and Cu/Cu_3P-N-CNFs. The C 1s core-level spectra of Cu-N-CNFs (Fig. S13a) could be deconvoluted into four subpeaks, including C-C/C = C, C-O/C–N, C=O, and O=C–O [47]. The four subpeaks in N 1s core levels for Cu-N-CNFs corresponded to pyridinic N, pyrrolic N, graphite N, and oxidized N (Fig. S13b) [42]. Similar C 1s and N 1s deconvoluted subpeaks could be seen for Cu_3P-N-CNFs (Fig. S13a and b) and Cu/Cu_3P-N-CNFs (Fig. 5c and d). In addition, P 2p core-levels of Cu_3P-N-CNFs (Fig. S13c) and Cu/Cu_3P-N-CNFs (Fig. 5e) were also deconvoluted, and the observed three subpeaks were assigned to P-Cu (~130.1 eV), P-C (~132.3 eV), and P-O (~134.2 eV), respectively [65]. To understand the chemical conversions for Cu/Cu_3P-N-CNFs during lithium insertion and to investigate the underline mechanism of enhanced electrochemical performance, the electrode was discharged to 0.8 V (at which the conversion reaction between Cu_3P and Li occurs [66,67]), the cell was disassembled and the electrodes were washed with solvent (DOL/DME), and then XPS measurements were also conducted. In the XPS spectra of discharged Cu/Cu_3P-N-CNFs, Cu and P signals became inconspicuous while additional S and F signals could be clearly detected due to the covering of residual LiTFSI. Consistently, the newly emerging peaks in C 1s, N 1s and P 2p spectra could be assigned to C-F (292.8 eV), NO_3^- (408.2 eV, $LiNO_3$ additive), P-Li (131.5 eV in Fig. 5b), respectively. Compared with the Cu/Cu_3P-N-CNFs in the initial stage, the main difference of discharged Cu/Cu_3P-N-CNFs was due to the introduction of NO_3^- (408.2 eV), which came from the $LiNO_3$ additive in the electrolyte. Pyridinic and pyrrolic N had been proved to exhibit strong affinity to Li both in theoretical calculation and experiments [68], which could reduce the energy barrier for Li nucleation. The relative electronegativity of graphitic N atoms reduces the electron density on the adjacent C nuclei, which helps electrons transfer from the adjacent C to N atoms, and N backdonates electrons to the adjacent C p_z orbitals [69]. Thus, the graphitic N atoms play the role of improving the conductivity of the frameworks, which is favorable to transport electrons in the electrode during the Li deposition [70]. According to the line sweep voltammetry measurements (Fig. S14b), the electrolyte salt (LiTFSI) was stable up to ~ 5.1 V, indicating that no significant decomposition occurred on the surface of Cu/Cu_3P-N-CNFs electrode. Moreover, due to the electrochemical reaction between lithium and Cu/Cu_3P heterostructures, Li-P bond was also observed in Li 1s spectrum, demonstrating the formation of ionic conductive lithium phosphide [48,71]. The generated lithium phosphide as one of the highly-ionic conductor (conductivity $\approx 10^{-4}$ S cm^{-1} at room temperature) [72] could enhance the transportation of Li^+, thus fast and homogenized Li^+ flux, as well as uniform Li plating are achieved [58,73]. However, no much difference could be detected in Cu 2p core-levels (Fig. S13d) for the four samples as the locations between Cu (0) and Cu (+1) were too close to be deconvoluted.

Symmetrical cells were then tested to further investigate the Li^+ transport capability and interfacial stability in different electrodes. Prior to the battery assembly, Li@Cu foil, Li@Cu-N-CNFs, Li@Cu_3P-N-CNFs, and Li@Cu/Cu_3P-N-CNFs electrodes were prepared by plating 5 mAh cm^{-2} of Li onto Cu foil, Cu-N-CNFs, Cu_3P-N-CNFs and Cu/Cu_3P-N-CNFs,

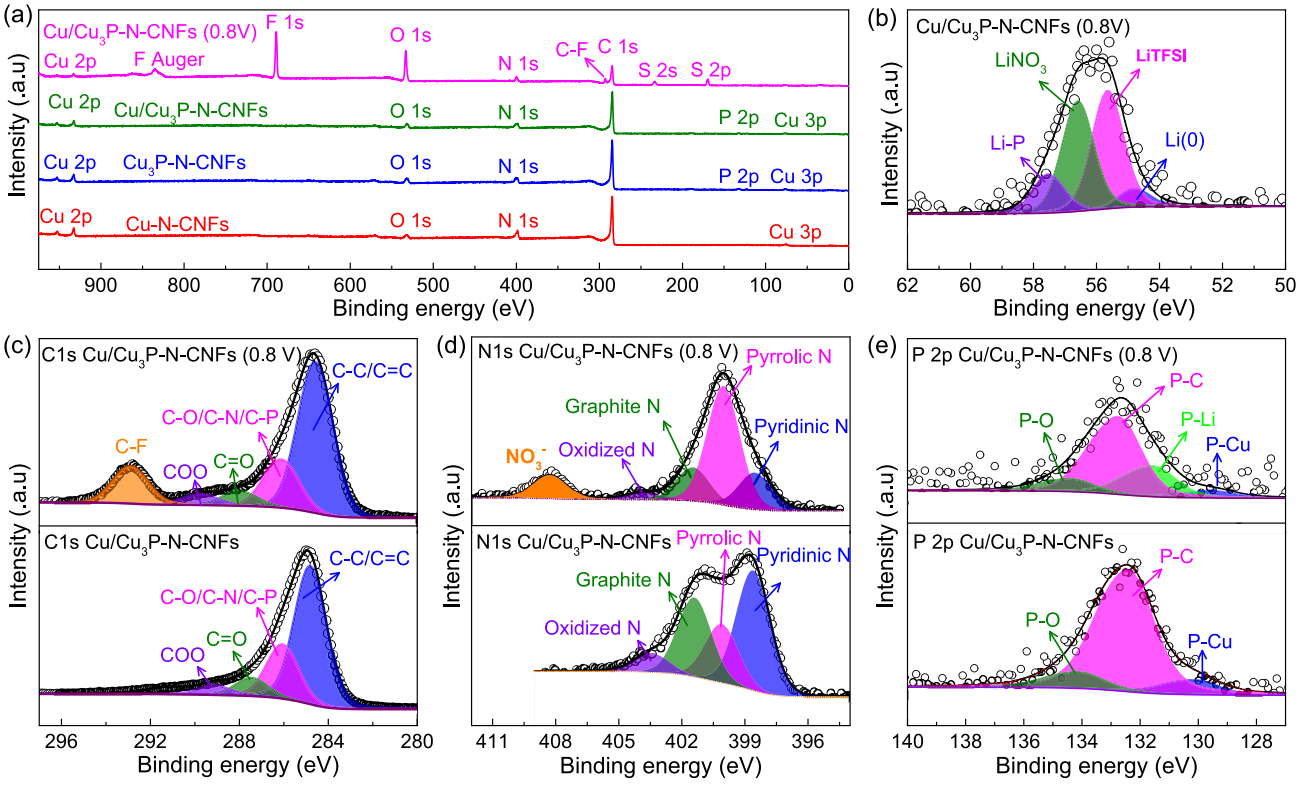

Fig. 5. XPS measurements of current collectors. (a) Full XPS spectra of Cu-N-CNFs, Cu_3P-N-CNFs, Cu/Cu_3P-N-CNFs, and Cu/Cu_3P-N-CNFs discharged to 0.8 V. (b) High-resolution Li 1s XPS spectrum of Cu/Cu_3P-N-CNFs discharged to 0.8 V. High-resolution (c) C 1s spectra, (d) N 1s spectra and (e) P 2p spectra of fresh and discharged Cu/Cu_3P-N-CNFs to 0.8 V, respectively.

respectively. The rate performances were tested from 0.5 mA cm^{-2} to 10 mA cm^{-2} with the fixed capacity of 1 mAh cm^{-2}. The Li@Cu/Cu_3P-N-CNFs electrodes delivered the lowest voltage hysteresis and the best rate performance at different current densities (Fig. 4c, Fig. S15c and d), which was slightly better than Li@Cu_3P-N-CNFs, and superior to Li@Cu-N-CNFs. On the contrary, much increased voltage hysteresis and obvious short circuit were detected for the Li@Cu electrode under high current density (>5 mA cm^{-2}) owing to its serious dendritic Li growth. According to the equation of Sand's time and Chazalviel's model, the higher current density could accelerate the growth rate of Li dendrites [74,75]. Besides good rate performances, Li@Cu/Cu_3P-N-CNFs assembled symmetrical cell also maintained a highly stable voltage profile as no obvious increased-voltage hysteresis was observed before 1494 h (747 cycles, Fig. 4d–g), and a small voltage hysteresis (~78 mV at 1 mA cm^{-2}, 1 mAh cm^{-2}) was retained. In comparison with the previously reported Li-metal anodes that configured with 3D skeletons (summarized in Table S2), the cyclic performance of symmetric cells assembled with Li@Cu/Cu_3P-N-CNFs electrode was still among the top results. However, Li@Cu_3P-N-CNFs cell exhibited a large voltage hysteresis of ~ 140 mV after 750 h cycling. With the repeated Li plating/stripping on Li@Cu_3P-N-CNFs, dead Li and Li dendrites gradually grew and accumulated on the surface of Li@Cu_3P-N-CNFs due to relatively ununiform Li deposition, which leaded to the gradually increased hysteresis voltage in Fig. 4f and finally short circuit after 800 h in Fig. 4d, and this phenomenon was also reported in previous work [18]. By sharp contrast, Li@Cu-N-CNFs and Li@Cu based cells demonstrated inferior cyclic performance, which could only survive 500 h and less than100 hours, respectively (Fig. S15e).

Thereafter, the developed lithium anodes (plated with 5 mAh cm^{-2} of Li) were paired with S@CNTs cathode to evaluate their potential application in Li-S full cells. The sulfur content of S@CNTs was confirmed to be ~ 71 wt% by TGA (Fig. S16g) and the sulfur loading on electrode was controlled at 1.2–1.4 mg cm^{-2}. Thus, the capacity ratio of lithium anode to sulfur cathode (assuming 100% utilization of sulfur) was as low as 2.1–2.5. Fig. 6a illustrates the rate performance of Li-S full cells from 0.1C to 2C (1C = 1675 mA g^{-1}). At the low current density of 0.1C, all three N-CNFs-based Li anodes delivered high discharge capacities (~1300 mAh/g), much higher than that of Li@Cu foil (1051 mAh/g). With increasing the current density, the capacity of Li@Cu/Cu_3P-N-CNFs gradually decreased and reached the highest capacity of 568 mAh/g at 2C, superior to that of Cu_3P-N-CNFs (494 mAh/g) and of Cu-N-CNFs (380 mAh/g). Consistent with the rate performance for symmetrical cells, Li@Cu foil assembled Li-S cell could only operate under low current density (0.1–0.5C), and it barely contributed to the discharge capacity at the high current density (2C). Charge/discharge curves for different electrodes are presented in Fig. 6b and Fig. S16a–c to

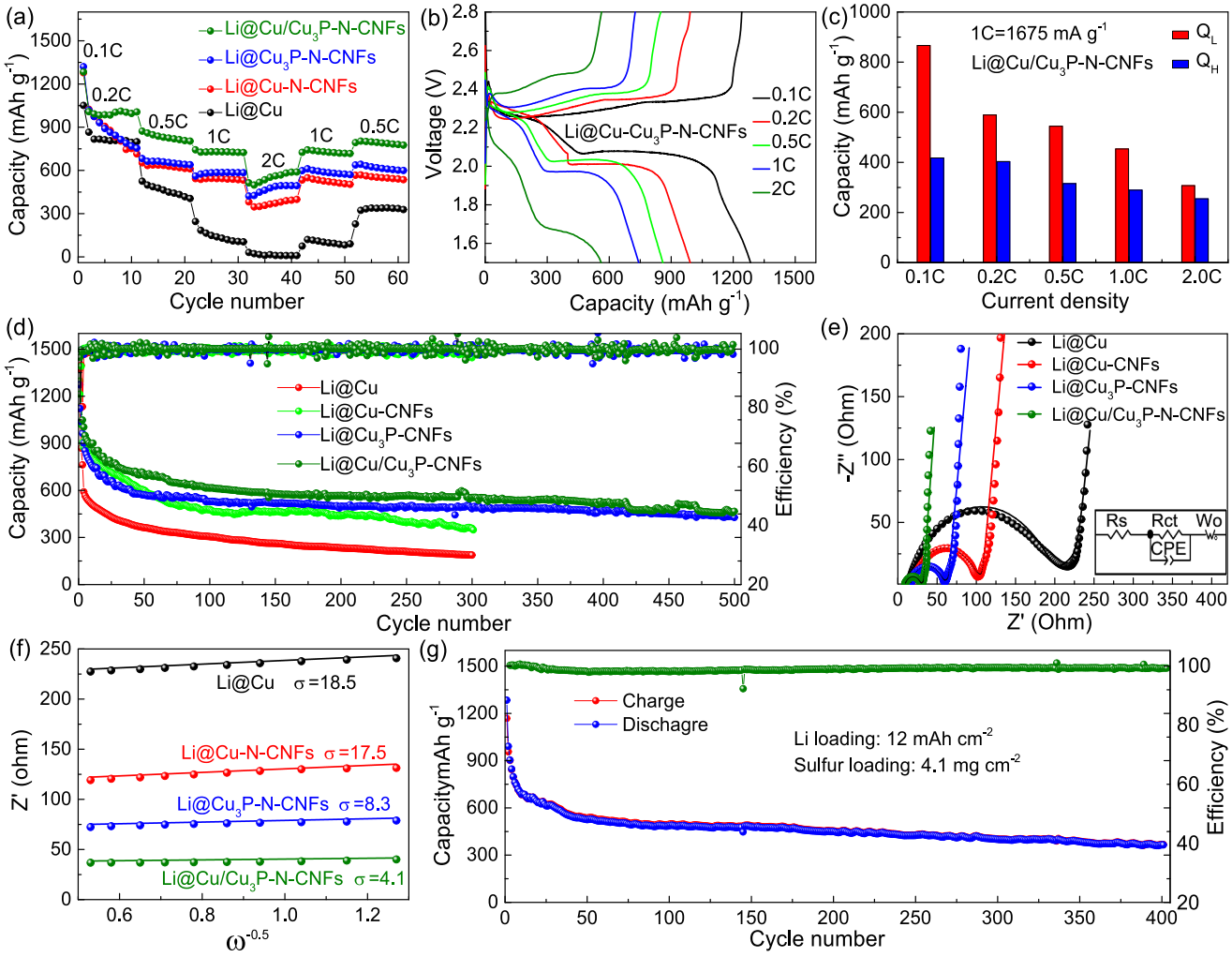

Fig. 6. Electrochemical performance of Li-S full cells assembled with different Li anodes. (a) rate performance. (b) Charge-discharge curves of Li-S cell assembled with Li@Cu/Cu_3P-N-CNFs anode. (c) Capacities contributed from high platform and low platform. (d) Cyclic performance at 0.2C. (e) EIS of the Li-S batteries configured with different Li anodes (the inset is the equivalent circuit; the lines are fitted impedance curve). (f) The relationship between Z' and $\omega^{-0.5}$ at low frequency. (g) Cyclic stability of Li-S battery assembled with Li@Cu/Cu_3P-N-CNFs anode (pre-deposited 12 mAh cm^{-2} Li) and high sulfur loading (4.1 mg cm^{-2}) cathode.

compare the lithiation/dilatation processes in Li-S cells. At the low current densities, the discharge curves of all Li-S cells displayed two plateaus that are at 2.4–2.1 V and 2.1–2.0 V, respectively, corresponding to the reduction of octa-atomic sulfur (S_8) to long-chain polysulfides (Li_2S_x, x = 4–8), and then from long-chain polysulfides to short-chain polysulfide(Li_2S_x, x = 2–3) and finally lithium sulfide, respectively [76,77]. In reverse, the plateau at 2.2–2.4 V in the charge curves was due to the oxidation of lithium sulfide to polysulfides and finally octa-atomic sulfur. However, the platforms in the discharge curves gradually moved to lower voltage while the platform in the charge curves moved to higher voltage with the increase of current density, indicating the increased electrode polarization [6]. In particular, no obvious platforms could be observed from the charge/discharge curves in Li@Cu based Li-S cell at the high current densities of 1C and 2C, which demonstrated the most serious polarization coming from the poor mass transport. The polarizations were affected comparatively lesser for N-CNFs-based Li anodes (especially the Li@Cu/Cu_3P-N-CNFs electrode) than those of Li@Cu anode, confirming the importance of dendritic-free 3D Li anodes for enhancing the performance of Li-S full batteries during fast charge–discharge. According to the electron transfer in reduction reaction, the upper-plateau reaction contributes ~ 25% of the overall capacity (Q_H: theoretical value = 419 mAh/g) while the lower-plateau reaction should provide ~ 75% (Q_L: theoretical value = 1256 mAh/g) [78]. As shown in Fig. 6c and Fig. S16d–f, the discharge capacities (Q_H and Q_L) of the electrodes under various current density were calculated to assess the two-plateau electrochemical reactions. For all the electrodes, their Q_L numbers decreased faster than Q_H with increasing the current density, indicating the capacity drop was mainly from Q_L drop due to the sluggish kinetics during the formation of insoluble lithium disulfide and lithium sulfide. Compared with the Li@Cu foil, both the Q_H and Q_L of Li@Cu/Cu_3P-N-CNFs anode decreased slower. Li@Cu-N-CNFs and Li@Cu_3P-N-CNFs electrode exhibited moderate and similar capacity decrease for the two plateaus under the high rates. It should be note that the upper-plateau capacity of Li@Cu/Cu_3P-N-CNFs was slightly higher than the theoretical value (419 mAh/g), which was commonly observed in the recent reports as compared in Table S3. The reasons for the excess capacity were as follows. At first, the current density was very low (0.1C), and the time is long enough for the adequate reduction of sulfur to polysulfides, leading to the high capacity. In addition, at such a low current density, stable SEI was likely to form on the Li@Cu/Cu_3P-N-CNFs anode, which could contribute to the consumption of electrolyte as well as the extra capacity [79]. Moreover, the stabilized and regulated Li@Cu/Cu_3P-N-CNFs anode was also beneficial for the Li^+ transportation and chemical conversion between Li^+ and sulfur, and for maintaining high capacity. To further elucidate the excess capacity and detect the components of SEI, the discharged Li@Cu/Cu_3P-N-CNFs anode was characterized by ex-situ XRD, XPS and TEM (Fig. 7d–k). However, due to the limitation of the ex-situ characterizations and the

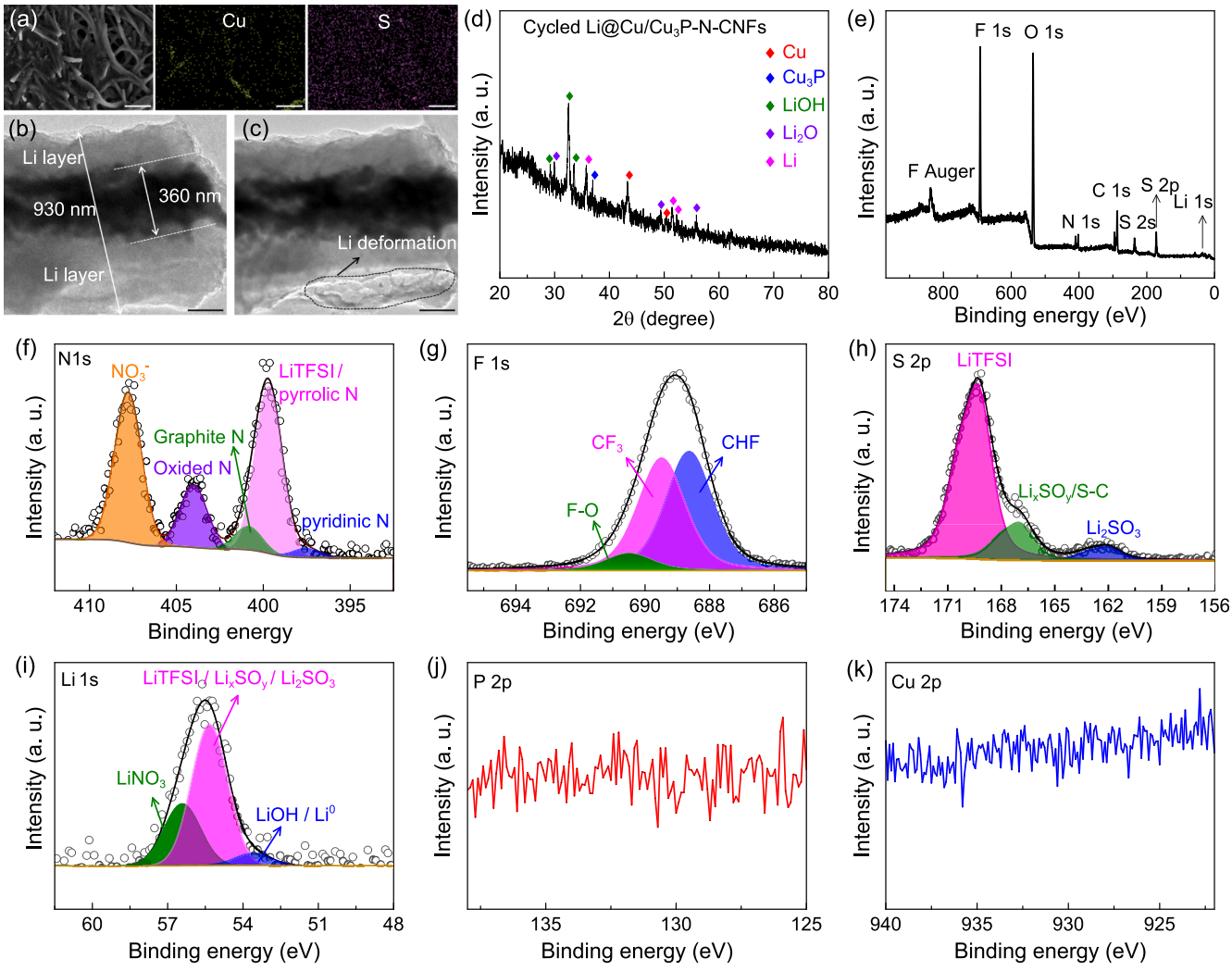

Fig. 7. Characterizations of Li@Cu/Cu_3P-N-CNFs after cycling in Li-S full cells. (a) SEM image and corresponding EDS mapping of Cu and S elements (the scale bars are 5 μm). (b, c) TEM image of Li@Cu/Cu_3P-N-CNFs electrode before and after electron beam focused, respectively (the scale bars are 200 nm). (d) XRD pattern. (e) Full XPS spectrum, and high resolution XPS spectra of (f) N 1s, (g) F 1s, (h) S 2p, (i) Li 1s, (j) P 2p and (k) Cu 2p core levels, respectively.

sensitivity of Li@Cu/Cu_3P-N-CNFs anode to water and air, it was hard to accurately analyze the components of SEI.

To explore the mechanism and explain the enhanced rate performance of Li-S cell assembled with Li@Cu/Cu_3P-N-CNFs anodes, the EIS of fresh Li-S batteries were compared in Fig. 6e. All the spectra were made up of a depressed semicircle in the high frequency region followed with a sloping line in the low frequency region, which are relevant to the resistances for charge-transfer process and mass-transfer process, respectively. The results were fitted through the equivalent circuit (the inset in Fig. 6e) and summarized in Table S1. The R_{ct} (resistance for charge transfer) of Li@Cu assembled cell was fitted to be 183.8 Ohm, much higher than those of Li@Cu-N-CNFs (83.9 Ohm), Li@Cu_3P-N-CNFs (42.1 Ohm) and Li@Cu/Cu_3P-N-CNFs (20.5 Ohm) equipped cells. In addition, the Li^+ ion diffusion coefficient (D) in Li-S batteries assembled with different anodes could be estimated based on the following formula [80]:

$$D = \frac{R^2T^2}{2A^2n^4F^4C^2\sigma^2} \quad (1)$$

where R is the gas constant (8.314 J mol^{-1} K^{-1}), T is the absolute temperature (298.15 K), A is the contact area of the electrode, n is the number of transferred electrons involved in the chemical reaction (n = 2), F is the Faraday's constant (96485.33C mol^{-1}), C is the concentration of lithium ion, and σ is the Warburg factor. The Warburg factor could be calculated based on the linear relationship between σ and Z' (the real component of the impedance) according to the following equation [81]:

$$Z' = R_s + R_{ct} + \sigma\omega^{-1/2} \quad (2)$$

where ω is the angular frequency ($\omega = 2\pi f$). As can be seen from Fig. 6f, Li@Cu assembled cell possessed the highest σ (18.5), slightly higher than that of Li@Cu-N-CNFs (17.5), reflecting a high resistance for Li^+ diffusion in these two electrodes. In comparison, the σ for Li@Cu_3P-N-CNFs (8.3) and Li@Cu/Cu_3P-N-CNFs (4.1) equipped cells was only a half and a quarter of that of Li@Cu, respectively. Combining the above two equations with fitted σ, the diffusivity of Li@Cu, Li@Cu-N-CNFs, Li@Cu_3P-N-CNFs, and Li@Cu/Cu_3P-N-CNFs assembled Li-S cells were calculated to be 5.07×10^{-10} cm^2 s^{-1}, 5.66×10^{-10} cm^2 s^{-1}, 2.52×10^{-9} cm^2 s^{-1}, and 1.03×10^{-8} cm^2 s^{-1}, respectively. The reduced charge transfer resistance and enhanced diffusion coefficient for Li@Cu/Cu_3P-N-CNFs assembled cell indicated the excellent interfacial compatibility between electrolyte and electrodes, leading to the lowest R_{ct}, highest diffusivity, as well as the fantastic electrochemical performance.

Long-term cyclic performance was also collected at 0.2C (cells were activated at 0.1C for the first cycle) to evaluate the stability of Li anodes in Li-S batteries. As shown in Fig. 6d, Li@Cu configurated battery showed the worst cyclic performance and the discharge capacity gradually decreased through the whole cyclic process due to the serious depletion of both limited Li anode and electrolyte, and only 187 mAh/g was retained after 300 cycles. For fabric Li anodes assembled batteries, the decrease of capacity occurred before 100 cycles mainly due to the dissolution and migration of polysulfides from S@CNTs cathodes. Thereafter the batteries could operate without obvious decay up to 230 cycles for Li@Cu-N-CNFs (425 mAh/g), and 500 cycles for both Li@Cu_3P-N-CNFs (432 mAh/g) and Li@Cu/Cu_3P-N-CNFs (458 mAh/g) anodes due to their stable 3D structures. Both Li@Cu_3P-N-CNFs and Li@Cu/Cu_3P-N-CNFs anodes demonstrated excellent stability in Li-S full cells. In comparison with the results from the symmetrical cells (Fig. 4d), the lower current density in Li-S full cells (~0.4 mA cm^{-2}) than that in the symmetrical cells (1 mA cm^{-2}) led to slower battery decay and longer lifespan (~1900 h) for both Cu_3P-based Li-S cells.

To assess the potential for practical application, high-capacity Li@Cu/Cu_3P-N-CNFs anodes (pre-deposited 12 mAh cm^{-2} of Li, Fig. S16h) were paired with high sulfur loading (4.1 mg cm^{-2}) cathodes. The battery was activated at 0.05C for the first cycle and the initial discharge capacity was as high as 1284 mAh/g (~5.8 mAh cm^{-2}, Fig. S16i), corresponding to the high utilization (~76% of sulfur and ~48% of Li anode) for the active materials. Then the battery was cycled at 0.2C as presented in Fig. 6g. A high discharge capacity of 991 mAh/g (~4.5 mAh cm^{-2}) was achieved for the second cycle at 0.2C. Moreover, high discharge capacity of 378 mAh/g (~1.8 mAh cm^{-2}) and high discharge plateau (~2.1 V) were maintained after 400 cycles, corresponding to a low decay rate of 0.15% per cycle. These results demonstrated the great potential of Li@Cu/Cu_3P-N-CNFs anode for the application in high-energy density Li-S full cells.

Furthermore, we tested the Li@Cu/Cu_3P-N-CNFs || S@CNTs full cells under lean electrolyte condition (5 μL or 7 μL electrolyte per milligram sulfur) and low N/P ratio (~2.6). Fig. S17 showed the cyclic performance of Li@Cu/Cu_3P-N-CNFs || S@CNTs full cells under lean electrolyte and low N/P conditions. The cells were activated at 0.05C for the initial 3 cycles and then cycled at 0.2C. The initial discharge capacities at 0.05C were 1059 mAh/g and 811 mAh/g of cells with 7 μL mg^{-1} and 5 μL mg^{-1} electrolyte per milligram sulfur (e/S ratio), respectively. When the current density was increased to 0.2C, the discharge capacities were decreased to 407.5 mAh/g and 353.1 mAh/g for the fourth cycle due to the lack of electrolyte and inadequate redox reactions. After 200 cycles, the cells with the e/S ratio of 7 μL mg^{-1} and 5 μL mg^{-1} stabilized at 434.3 mAh/g and 354.4 mAh/g, respectively. The stable cyclic performance could be attributed to the following reasons. At first, the Li@Cu/Cu_3P-N-CNFs anode alleviated the repeated formation of unstable SEI, leading to the reduced consumption of electrolyte and Li anode. In addition, the polysulfide migration was also alleviated with the limited electrolyte, which further contributed to the stable cycling of the Li-S full cells.

To detected the possible reactions between the migrated polysulfides and Cu in Cu/Cu_3P-N-CNFs, and evaluate the structural stability of Li@Cu/Cu_3P-N-CNFs, the cycled cells were disassembled and Li@Cu/Cu_3P-N-CNFs were characterized. As seen from the SEM image (Fig. 7a), the surface was not smooth due to the deposition of Li and the polysulfides that escaped from the S@CNTs cathodes. In addition, Cu element (0.4 at. %) and P element (0%) were hardly detected due to the coverage of Li metal and sulfur species, and the limited detecting depth of EDS. Similarly, Cu and P singles were hardly detected from the XPS measurements (Fig. 7e, j and k). The high-resolution XPS spectra of N 1s, F 1s, S 2p, and Li 1s core levels were fitted and presented in Fig. 7f–i. Compared to the pristine Cu/Cu_3P-N-CNFs, all the deconvoluted peaks could be attributed to the singles that arisen from LiTFSI, $LiNO_3$, deposited Li, or oxidized Li (during the transfer), which confirmed that there was no reaction between polysulfides and Cu in Cu/Cu_3P-N-CNFs. In the XRD pattern of cycled Li@Cu/Cu_3P-N-CNFs (Fig. 7d), the peaks could be attributed to Cu, Cu_3P, LiOH, Li_2O and Li. No diffraction peak of compounds that made up of copper and sulfur elements could be detected. As seen from the TEM image in Fig. 7b, the diameter of cycled Li@Cu/Cu_3P-N-CNFs (~940 nm) was much larger than that of the pristine Cu/Cu_3P-N-CNFs (~360 nm) due to the deposited Li metal (the Li layer was robust even after the sonication during the preparation of TEM sample) and sulfur species. We tried to capture some HRTEM images, but the focus of high-energy electron bean damaged the Li layer and led to the serious deformation (Fig. 7c). Thus, there was no reactions between polysulfides and Cu in Cu/Cu_3P-N-CNFs, and the reasons of which were as follows. The electrodeposition of Li on Cu/Cu_3P-N-CNFs was uniform, leading to the formation of compact and dense Li coating layer and solid electrolyte interface (SEI) on the surface. During the cycling of Li@Cu/Cu_3P-N-CNFs || S@CNTs full cells, the real capacity ratio of Li anode to sulfur cathode was 2.6. Only a small part of Li uniformly stripped from Li@Cu/Cu_3P-N-CNFs even at the fully discharged state, which indicated that there were still dense SEI and robust Li coating layers on Cu/Cu_3P-N-CNFs to avoid the reactions between polysulfides and Cu in Cu/Cu_3P-N-CNFs. These observations further demonstrated the uniform Li plating/stripping on Cu/Cu_3P-N-CNFs as well as the excellent stability of the corresponding Li@Cu/Cu_3P-N-CNFs

anode.

4. Conclusions

In summary, we designed Cu/Cu_3P-N-CNFs as a 3D lithiophilic host for a robust and dendrite-free Li metal anodes. The 3D hierarchical porous structure has a high specific surface area that can alleviate the huge volume variation during Li plating/stripping processes and reduce the local current density. The lithiophilic nitrogen-doped carbon sites and the embedded functional Cu/Cu_3P heterostructure endow ultralow nucleation overpotential and small polarization. As a result, the nucleation and growth behavior of Li on the Cu/Cu_3P-N-CNFs are effectively regulated. The Cu/Cu_3P-N-CNFs electrodes exhibit high Coulombic efficiency (~94%) for 500 cycles at 1 mA cm^{-2} with the capacity of 1 mAh cm^{-2}. Moreover, the Li@Cu/Cu_3P-N-CNFs assembled symmetric cells show remarkable cycling stability up to 1500 h (1 mA cm^{-2} for 1 mAh cm^{-2}) with an ultralow voltage hysteresis and superior rate capability up to 10 mA cm^{-2} (for 1 mAh cm^{-2}). The Li-S full cells made of the Li@Cu/Cu_3P-N-CNFs anode and the S@CNTs cathode also exhibit desirable rate capability and stable cycle life. These excellent electrochemical properties endow the Cu/Cu_3P-N-CNFs to be a highly promising host for stabilizing metallic Li anodes. This work is expected to create new inspiration for the design and fabrication of multi-functional 3D frameworks for stabilizing other alkali such as sodium or potassium metal anodes.

Declaration of Competing Interest

The authors declare that they have no known competing financial interests or personal relationships that could have appeared to influence the work reported in this paper.

Data availability

Data will be made available on request.

Acknowledgements

Yinyu Xiang greatly thanks the China Scholarship Council for his PhD Scholarship (CSC No. 201806950083). The authors gratefully acknowledge the financial support from the Faculty of Science and Engineering, University of Groningen, the Netherlands. The authors thank Minpeng Liang for his support with the Raman measurements, Jianwu Sun for his help for SEM tests, and Diego Ribas Gomes, and Marc C.A. Stuart for their help for the TEM characterizations.

Appendix A. Supplementary data

Supplementary data to this article can be found online at https://doi.org/10.1016/j.cej.2023.145089.

References

[1] A. Manthiram, Y. Fu, S.-H. Chung, C. Zu, Y.-S. Su, Rechargeable Lithium-Sulfur Batteries, Chem. Rev. 114 (23) (2014) 11751–11787, https://doi.org/10.1021/cr500062v.
[2] Z.J. Zhang, Z.H. Fang, Y.Y. Xiang, D. Liu, Z.Z. Xie, D.Y. Qu, M.L. Sun, H.L. Tang, J. S. Li, Cellulose-Based Material in Lithium-Sulfur Batteries: A Review, Carbohydr. Polym. 255 (2021), 117469, https://doi.org/10.1016/j.carbpol.2020.117469.
[3] Y.Y. Xiang, J.S. Li, J.H. Lei, D. Liu, Z.Z. Xie, D.Y. Qu, K. Li, T.F. Deng, H.L. Tang, Advanced Separators for Lithium-Ion and Lithium-Sulfur Batteries: A Review of Recent Progress, ChemSusChem 9 (21) (2016) 3023–3039, https://doi.org/10.1002/cssc.201600943.
[4] X.B. Cheng, R. Zhang, C.Z. Zhao, Q. Zhang, Toward Safe Lithium Metal Anode in Rechargeable Batteries: A Review, Chem. Rev. 117 (15) (2017) 10403–10473, https://doi.org/10.1021/acs.chemrev.7b00115.
[5] J. Wang, G. Li, D. Luo, Y. Zhang, Y. Zhao, G. Zhou, L. Shui, X. Wang, Z. Chen, Engineering the Conductive Network of Metal Oxide-Based Sulfur Cathode toward Efficient and Longevous Lithium-Sulfur Batteries, Adv. Energy Mater. 10 (41) (2020) 2002076, https://doi.org/10.1002/aenm.202002076.
[6] R. Liu, W. Liu, Y. Bu, W. Yang, C. Wang, C. Priest, Z. Liu, Y. Wang, J. Chen, Y. Wang, J. Cheng, X. Lin, X. Feng, G. Wu, Y. Ma, W. Huang, Conductive Porous Laminated Vanadium Nitride as Carbon-Free Hosts for High-Loading Sulfur Cathodes in Lithium-Sulfur Batteries, ACS Nano 14 (12) (2020) 17308–17320, https://doi.org/10.1021/acsnano.0c07415.
[7] F. Shi, L. Zhai, Q. Liu, J. Yu, S.P. Lau, B.Y. Xia, Z.-L. Xu, Emerging Catalytic Materials for Practical Lithium-Sulfur Batteries, J. Energy Chem. 76 (2023) 127–145, https://doi.org/10.1016/j.jechem.2022.08.027.
[8] Q. Zhang, Y. Qian, J.-J. Zou, R. Gao, H. Yang, Tandem Co–O Dual Sites on Halloysite with Promoted Reaction Kinetics for Sulfur Reduction, J. Energy Chem. 75 (2022) 486–493, https://doi.org/10.1016/j.jechem.2022.09.011.
[9] Y.Y. Xiang, Z. Wang, W.J. Qiu, Z.R. Guo, D. Liu, D.Y. Qu, Z.Z. Xie, H.L. Tang, J. S. Li, Interfacing Soluble Polysulfides with a SnO_2 Functionalized Separator: An Efficient Approach for Improving Performance of Li-S Battery, J. Membr. Sci. 563 (2018) 380–387, https://doi.org/10.1016/j.memsci.2018.06.004.
[10] Z. Fang, L. Tu, Z. Zhang, J. Wei, Y. Xiang, W. Guo, J. Li, Simultaneously Suppressing the Dendritic Lithium Growth and Polysulfides Migration by a Polyethyleneimine Grafted Bacterial Cellulose Membrane in Lithium-Sulfur Batteries, Appl. Surf. Sci. 597 (2022), 153683, https://doi.org/10.1016/j.apsusc.2022.153683.
[11] J. Wang, W. Cai, X. Mu, L. Han, N.a. Wu, C. Liao, Y. Kan, Y. Hu, Construction of Multifunctional and Flame Retardant Separator Towards Stable Lithium-Sulfur Batteries with High Safety, Chem. Eng. J. 416 (2021) 129087, https://doi.org/10.1016/j.cej.2021.129087.
[12] M. Hu, Q. Ma, Y. Yuan, Y. Pan, M. Chen, Y. Zhang, D. Long, Grafting Polyethyleneimine on Electrospun Nanofiber Separator to Stabilize Lithium Metal Anode for Lithium Sulfur Batteries, Chem. Eng. J. 388 (2020) 124258, https://doi.org/10.1016/j.cej.2020.124258.
[13] A.M. Abraham, T. Boteju, S. Ponnurangam, V. Thangadurai, A Global Design Principle for Polysulfide Electrocatalysis in Lithium-Sulfur Batteries—a Computational Perspective, Battery Energy 1 (3) (2022), 20220003, https://doi.org/10.1002/bte2.20220003.
[14] S. Thieme, J. Brueckner, A. Meier, I. Bauer, K. Gruber, J. Kaspar, A. Helmer, H. Althues, M. Schmuck, S. Kaskel, A Lithium-Sulfur Full Cell with Ultralong Cycle Life: Influence of Cathode Structure and Polysulfide Additive, J. Mater. Chem. A 3 (7) (2015) 3808–3820, https://doi.org/10.1039/c4ta06748g.
[15] H.-L. Wu, M. Shin, Y.-M. Liu, K.A. See, A.A. Gewirth, Thiol-Based Electrolyte Additives for High-Performance Lithium-Sulfur Batteries, Nano Energy 32 (2017) 50–58, https://doi.org/10.1016/j.nanoen.2016.12.015.
[16] Q. Guo, Z. Zheng, Rational Design of Binders for Stable Li-S and Na-S Batteries, Adv. Funct. Mater. 30 (6) (2019) 1907931, https://doi.org/10.1002/adfm.201907931.
[17] Y. Huang, M. Shaibani, T.D. Gamot, M. Wang, P. Jovanović, M.C. Dilusha Cooray, M.S. Mirshekarloo, R.J. Mulder, N.V. Medhekar, M.R. Hill, M. Majumder, A Saccharide-Based Binder for Efficient Polysulfide Regulations in Li-S Batteries, Nat. Commun. 12 (1) (2021) 5375, https://doi.org/10.1038/s41467-021-25612-5.
[18] S. Zhang, D. Wang, X. Xu, H. Li, W. Xu, Y. Ma, B. Wang, L. Zhi, X. Li, Spatially Hierarchical Carbon Enables Superior Long-Term Cycling of Ultrahigh Areal Capacity Lithium Metal Anodes, Matter 5 (4) (2022) 1263–1276, https://doi.org/10.1016/j.matt.2022.01.017.
[19] X. Xiong, W. Yan, Y. Zhu, L. Liu, L. Fu, Y. Chen, N. Yu, Y. Wu, B. Wang, R. Xiao, $Li_4Ti_5O_{12}$ Coating on Copper Foil as Ion Redistributor Layer for Stable Lithium Metal Anode, Adv. Energy Mater. 12 (13) (2022) 2103112, https://doi.org/10.1002/aenm.202103112.
[20] A. Manthiram, J. He, A. Bhargav, Covalent Organic Framework as an Efficient Protection Layer for Stable Lithium-Metal Anode, Angew. Chem. Int. Ed. Engl. 61 (18) (2022), e202116586, https://doi.org/10.1002/anie.202116586.
[21] D. Wang, C. Luan, W. Zhang, X. Liu, L. Sun, Q. Liang, T. Qin, Z. Zhao, Y. Zhou, P. Wang, W. Zheng, Zipper-Inspired Sei Film for Remarkably Enhancing the Stability of Li Metal Anode Via Nucleation Barriers Controlled Weaving of Lithium Pits, Adv. Energy Mater. 8 (21) (2018) 1800650, https://doi.org/10.1002/aenm.201800650.
[22] Y. Zhao, M. Amirmaleki, Q. Sun, C. Zhao, A. Codirenzi, L.V. Goncharova, C. Wang, K. Adair, X. Li, X. Yang, F. Zhao, R. Li, T. Filleter, M. Cai, X. Sun, Natural Sei-Inspired Dual-Protective Layers Via Atomic/Molecular Layer Deposition for Long-Life Metallic Lithium Anode, Matter 1 (5) (2019) 1215–1231, https://doi.org/10.1016/j.matt.2019.06.020.
[23] H. Zhang, L. Zhou, X. Du, J. Zhang, S. Tian, T. Liu, J. Zhang, S. Hu, W. Song, X. Zhou, G. Cui, Cyanoethyl Cellulose-Based Eutectogel Electrolyte Enabling High-Voltage-Tolerant and Ion-Conductive Solid-State Lithium Metal Batteries, Carbon Energy 4 (6) (2022) 1093–1106, https://doi.org/10.1002/cey2.227.
[24] B. Xu, X. Li, C. Yang, Y. Li, N.S. Grundish, P.-H. Chien, K. Dong, I. Manke, R. Fang, N. Wu, H. Xu, A. Dolocan, J.B. Goodenough, Interfacial Chemistry Enables Stable Cycling of All-Solid-State Li Metal Batteries at High Current Densities, J. Am. Chem. Soc. 143 (17) (2021) 6542–6550, https://doi.org/10.1021/jacs.1c00752.
[25] Y. Wang, C.J. Zanelotti, X. Wang, R. Kerr, L. Jin, W.H. Kan, T.J. Dingemans, M. Forsyth, L.A. Madsen, Solid-State Rigid-Rod Polymer Composite Electrolytes with Nanocrystalline Lithium Ion Pathways, Nat. Mater. 20 (9) (2021) 1255–1263, https://doi.org/10.1038/s41563-021-00995-4.
[26] L. Zhang, N. Deng, J. Kang, X. Wang, H. Gao, Y. Liu, H. Wang, G. Wang, B. Cheng, W. Kang, Enhanced Ionic Conductivity in a Novel Composite Electrolyte Based on Gd-Doped SnO_2 Nanotubes for Ultra-Long-Life All-Solid-State Lithium Metal Batteries, J. Energy Chem. 77 (2023) 326–337, https://doi.org/10.1016/j.jechem.2022.11.003.

[27] S. Ni, S. Tan, Q. An, L. Mai, Three Dimensional Porous Frameworks for Lithium Dendrite Suppression, J. Energy Chem. 44 (2020) 73–89, https://doi.org/10.1016/j.jechem.2019.09.031.

[28] C. Tang, H.-F. Wang, J.-Q. Huang, W. Qian, F. Wei, S.-Z. Qiao, Q. Zhang, 3D Hierarchical Porous Graphene-Based Energy Materials: Synthesis, Functionalization, and Application in Energy Storage and Conversion, Electrochem. Energy Rev. 2 (2) (2019) 332–371, https://doi.org/10.1007/s41918-019-00033-7.

[29] L. Liu, Y.X. Yin, J.Y. Li, N.W. Li, X.X. Zeng, H. Ye, Y.G. Guo, L.J. Wan, Free-Standing Hollow Carbon Fibers as High-Capacity Containers for Stable Lithium Metal Anodes, Joule 1 (3) (2017) 563–575, https://doi.org/10.1016/j.joule.2017.06.004.

[30] Y. Xiang, L. Lu, A.G.P. Kottapalli, Y. Pei, Status and Perspectives of Hierarchical Porous Carbon Materials in Terms of High-Performance Lithium-Sulfur Batteries, Carbon Energy 4 (3) (2022) 346–398, https://doi.org/10.1002/cey2.185.

[31] Z. Song, Z. Zhang, A. Du, S. Dong, G. Li, G. Cui, Uniform Magnesium Electrodeposition Via Synergistic Coupling of Current Homogenization, Geometric Confinement, and Chemisorption Effect, Adv. Mater. 33 (26) (2021), 2100224, https://doi.org/10.1002/adma.202100224.

[32] J. Zhang, Z. Chang, Z. Zhang, A. Du, S. Dong, Z. Li, G. Li, G. Cui, Current Design Strategies for Rechargeable Magnesium-Based Batteries, ACS Nano 15 (10) (2021) 15594–15624, https://doi.org/10.1021/acsnano.1c06530.

[33] L. Liu, Y.X. Yin, J.Y. Li, S.H. Wang, Y.G. Guo, L.J. Wan, Uniform Lithium Nucleation/Growth Induced by Lightweight Nitrogen-Doped Graphitic Carbon Foams for High-Performance Lithium Metal Anodes, Adv. Mater. 30 (10) (2018) 1706216, https://doi.org/10.1002/adma.201706216.

[34] D. Li, S. Zhang, Q. Zhang, P. Kaghazchi, H. Qi, J. Liu, Z. Guo, L. Wang, Y. Wang, Pencil-Drawing on Nitrogen and Sulfur Co-Doped Carbon Paper: An Effective and Stable Host to Pre-Store Li for High-Performance Lithium-Air Batteries, Energy Storage Mater. 26 (2019) 593–603, https://doi.org/10.1016/j.ensm.2019.12.003.

[35] Z. Xu, L. Xu, Z. Xu, Z. Deng, X. Wang, N, O-Codoped Carbon Nanosheet Array Enabling Stable Lithium Metal Anode, Adv. Funct. Mater. 31 (40) (2021) 2102354, https://doi.org/10.1002/adfm.202102354.

[36] Y. Fang, Y. Zeng, Q. Jin, X.F. Lu, D. Luan, X. Zhang, X.W. Lou, Nitrogen-Doped Amorphous Zn-Carbon Multichannel Fibers for Stable Lithium Metal Anodes, Angew. Chem. Int. Ed. Engl. 60 (15) (2021) 8515–8520, https://doi.org/10.1002/anie.202100471.

[37] Y. Fang, S.L. Zhang, Z.-P. Wu, D. Luan, X.W. Lou, A Highly Stable Lithium Metal Anode Enabled by Ag Nanoparticle-Embedded Nitrogen-Doped Carbon Macroporous Fibers, Sci. Adv. 7 (21) (2021) eabg3626, https://doi.org/10.1126/sciadv.abg3626.

[38] C.P. Yang, Y.G. Yao, S.M. He, H. Xie, E. Hitz, L.B. Hu, Ultrafine Silver Nanoparticles for Seeded Lithium Deposition toward Stable Lithium Metal Anode, Adv. Mater. 29 (38) (2017) 1702714, https://doi.org/10.1002/adma.201702714.

[39] C. Chen, J. Guan, N.W. Li, Y. Lu, D. Luan, C.H. Zhang, G. Cheng, L. Yu, X.W.D. Lou, Lotus-Root-Like Carbon Fibers Embedded with Ni-Co Nanoparticles for Dendrite-Free Lithium Metal Anodes, Adv. Mater. 33 (24) (2021), e2100608, https://doi.org/10.1002/adma.202100608.

[40] P. Zhai, L. Liu, Y. Wei, J. Zuo, Z. Yang, Q. Chen, F. Zhao, X. Zhang, Y. Gong, Self-Healing Nucleation Seeds Induced Long-Term Dendrite-Free Lithium Metal Anode, Nano Lett. 21 (18) (2021) 7715–7723, https://doi.org/10.1021/acs.nanolett.1c02521.

[41] H. Yuan, J. Nai, Y. Fang, G. Lu, X. Tao, X.W. Lou, Double-Shelled C@MoS_2 Structures Preloaded with Sulfur: An Additive Reservoir for Stable Lithium Metal Anodes, Angew. Chem. Int. Ed. Engl. 59 (37) (2020) 15839–15843, https://doi.org/10.1002/anie.202001989.

[42] C. Fu, W. Xu, C. Tao, L. Wang, T. Liu, Lithiophilic Nickel Phosphide Modifying Carbon Nanofibers for a Highly Reversible Lithium-Metal Anode, ACS Appl. Energy Mater. 5 (4) (2022) 4733–4742, https://doi.org/10.1021/acsaem.2c00148.

[43] X. Chen, X.-R. Chen, T.-Z. Hou, B.-Q. Li, X.-B. Cheng, R. Zhang, Q. Zhang, Lithiophilicity Chemistry of Heteroatom-Doped Carbon to Guide Uniform Lithium Nucleation in Lithium Metal Anodes, Sci. Adv. 5 (2) (2019) eaau7728, https://doi.org/10.1126/sciadv.aau7728.

[44] K. Yan, Z. Lu, H.-W. Lee, F. Xiong, P.-C. Hsu, Y. Li, J. Zhao, S. Chu, Y. Cui, Selective Deposition and Stable Encapsulation of Lithium through Heterogeneous Seeded Growth, Nat. Energy 1 (3) (2016) 16010, https://doi.org/10.1038/nenergy.2016.10.

[45] J. Liu, J. Zhang, Z. Zhang, A. Du, S. Dong, Z. Zhou, X. Guo, Q. Wang, Z. Li, G. Li, G. Cui, Epitaxial Electrocrystallization of Magnesium Via Synergy of Magnesiophilic Interface, Lattice Matching, and Electrostatic Confinement, ACS Nano 16 (6) (2022) 9894–9907, https://doi.org/10.1021/acsnano.2c04135.

[46] J. Liu, Z. Zhou, M. Wang, J. Zhang, Z. Li, G. Li, F. Li, G. Cui, Z. Zhang, Intercalation Species Regulation in Layered Vanadium Oxide Scaffolds Enables Long Cycle Life Mg-Metal Anodes, Chem. Eng. J. 466 (2023), 143308, https://doi.org/10.1016/j.cej.2023.143308.

[47] C. Fu, S. Lin, C. Zhao, J. Wang, L. Wang, J.L. Bao, Y. Wang, T. Liu, Li Migration, Nucleation and Growth Behavior Regulated by a Lithiophilic Cobalt Phosphide-Doped Carbon Nanofibers Derived Ion/Electron Conductive Framework, Energy Storage Mater. 45 (2021) 1109–1119, https://doi.org/10.1016/j.ensm.2021.11.009.

[48] J. Lin, C. Zeng, X. Lin, C. Xu, C.-Y. Su, Cnt-Assembled Octahedron Carbon-Encapsulated Cu_3P/Cu Heterostructure by in Situ Mof-Derived Engineering for Superior Lithium Storage: Investigations by Experimental Implementation and First-Principles Calculation, Adv. Sci. 7 (14) (2020) 2000736, https://doi.org/10.1002/advs.202000736.

[49] M.S. Seifner, M. Snellman, O.A. Makgae, K. Kumar, D. Jacobsson, M. Ek, K. Deppert, M.E. Messing, K.A. Dick, Interface Dynamics in Ag–Cu_3P Nanoparticle Heterostructures, J. Am. Chem. Soc. 144 (1) (2022) 248–258, https://doi.org/10.1021/jacs.1c09179.

[50] D. Yang, Y. Sun, Z. Tong, Y. Tian, Y. Li, Z. Jiang, Synthesis of Ag/TiO_2 Nanotube Heterojunction with Improved Visible-Light Photocatalytic Performance Inspired by Bioadhesion, J. Phys. Chem. C 119 (11) (2015) 5827–5835, https://doi.org/10.1021/jp511948p.

[51] J.S. DuChene, B.C. Sweeny, A.C. Johnston-Peck, D. Su, E.A. Stach, W.D. Wei, Prolonged Hot Electron Dynamics in Plasmonic-Metal/Semiconductor Heterostructures with Implications for Solar Photocatalysis, Angew. Chem. Int. Ed. Engl. 53 (30) (2014) 7887–7891, https://doi.org/10.1002/anie.201404259.

[52] Z. Shi, Z. Sun, X. Yang, C. Lu, S. Li, X. Yu, Y. Ding, T. Huang, J. Sun, Synergizing Conformal Lithiophilic Granule and Dealloyed Porous Skeleton toward Pragmatic Li Metal Anodes, Small Science 2 (5) (2022) 2100110, https://doi.org/10.1002/smsc.202100110.

[53] F. Shahbaz Tehrani, V. Daadmehr, A.T. Rezakhani, R. Hosseini Akbarnejad, S. Gholipour, Structural, Magnetic, and Optical Properties of Zinc- and Copper-Substituted Nickel Ferrite Nanocrystals, J. Supercond. Novel Magnet. 25 (7) (2012) 2443–2455, https://doi.org/10.1007/s10948-012-1655-5.

[54] G. Kresse, J. Furthmüller, Efficient Iterative Schemes for Ab Initio Total-Energy Calculations Using a Plane-Wave Basis Set, PhRvB 54 (16) (1996) 11169–11186, https://doi.org/10.1103/PhysRevB.54.11169.

[55] L. Zhang, X. Yin, S. Shen, Y. Liu, T. Li, H. Wang, X. Lv, X. Qin, S.W. Chiang, Y. Fu, F. Kang, B. Li, Simultaneously Homogenized Electric Field and Ionic Flux for Reversible Ultrahigh-Areal-Capacity Li Deposition, Nano Lett. 20 (8) (2020) 5662–5669, https://doi.org/10.1021/acs.nanolett.0c00797.

[56] H. Yuan, J. Nai, H. Tian, Z. Ju, W. Zhang, Y. Liu, X. Tao, X.W. Lou, An Ultrastable Lithium Metal Anode Enabled by Designed Metal Fluoride Spansules, Sci. Adv. 6 (10) (2020) eaaz3112, https://doi.org/10.1126/sciadv.aaz3112.

[57] Y. Liu, X. Tao, Y. Wang, C. Jiang, C. Ma, O. Sheng, G. Lu, X.W. Lou, Self-Assembled Monolayers Direct a Lif-Rich Interphase toward Long-Life Lithium Metal Batteries, Science 375 (6582) (2022) 739–745, https://doi.org/10.1126/science.abn1818.

[58] C. Sun, A. Lin, W. Li, J. Jin, Y. Sun, J. Yang, Z. Wen, In Situ Conversion of Cu_3P Nanowires to Mixed Ion/Electron-Conducting Skeleton for Homogeneous Lithium Deposition, Adv. Energy Mater. 10 (3) (2019) 1902989, https://doi.org/10.1002/aenm.201902989.

[59] S. Vijayan, R. Narasimman, K. Prabhakaran, A Urea Crystal Templating Method for the Preparation of Porous Alumina Ceramics with the Aligned Pores, J. Eur. Ceram. Soc. 33 (10) (2013) 1929–1934, https://doi.org/10.1016/j.jeurceramsoc.2013.02.031.

[60] A. Yabuki, N. Arriffin, Electrical Conductivity of Copper Nanoparticle Thin Films Annealed at Low Temperature, Thin Solid Films 518 (23) (2010) 7033–7037, https://doi.org/10.1016/j.tsf.2010.07.023.

[61] X. Peng, Y. Lv, S. Zhao, Chemical Vapor Deposition and Thermal Oxidation of Cuprous Phosphide Nanofilm, Coatings 12 (1) (2022) 68, https://doi.org/10.3390/coatings12010068.

[62] S. Li, H. Zhu, Y. Liu, Z. Han, L. Peng, S. Li, C. Yu, S. Cheng, J. Xie, Codoped Porous Carbon Nanofibres as a Potassium Metal Host for Nonaqueous K-Ion Batteries, Nat. Commun. 13 (1) (2022) 4911, https://doi.org/10.1038/s41467-022-32660-y.

[63] Z. Zhang, J. Wang, X. Yan, S. Zhang, W. Yang, Z. Zhuang, W.-Q. Han, In-Situ Growth of Hierarchical N-Doped CNTs/Ni Foam Scaffold for Dendrite-Free Lithium Metal Anode, Energy Storage Mater. 29 (2020) 332–340, https://doi.org/10.1016/j.ensm.2020.04.022.

[64] C. Yan, Y.-X. Yao, X. Chen, X.-B. Cheng, X.-Q. Zhang, J.-Q. Huang, Q. Zhang, Lithium Nitrate Solvation Chemistry in Carbonate Electrolyte Sustains High-Voltage Lithium Metal Batteries, Angew. Chem. Int. Ed. 57 (43) (2018) 14055–14059, https://doi.org/10.1002/anie.201807034.

[65] E. Jiang, J. Jiang, G. Huang, Z. Pan, X. Chen, G. Wang, S. Ma, J. Zhu, P.K. Shen, Porous Nanosheets of Cu_3P@N, P Co-Doped Carbon Hosted on Copper Foam as an Efficient and Ultrastable Ph-Universal Hydrogen Evolution Electrocatalyst, Sustain. Energy Fuels 5 (9) (2021) 2451–2457, https://doi.org/10.1039/D1SE00161B.

[66] S. Ni, J. Ma, X. Lv, X. Yang, L. Zhang, The Fine Electrochemical Performance of Porous Cu_3P/Cu and the High Energy Density of Cu_3P as Anode for Li-Ion Batteries, J. Mater. Chem. A 2 (48) (2014) 20506–20509, https://doi.org/10.1039/C4TA03871A.

[67] S. Ni, B. Zheng, J. Liu, D. Chao, X. Yang, Z. Shen, J. Zhao, Self-Adaptive Electrochemical Reconstruction Boosted Exceptional Li^+ Ion Storage in a Cu_3P@C Anode, J. Mater. Chem. A 6 (39) (2018) 18821–18826, https://doi.org/10.1039/C8TA04959A.

[68] R. Zhang, X.-R. Chen, X. Chen, X.-B. Cheng, X.-Q. Zhang, C. Yan, Q. Zhang, Lithiophilic Sites in Doped Graphene Guide Uniform Lithium Nucleation for Dendrite-Free Lithium Metal Anodes, Angew. Chem. Int. Ed. 56 (27) (2017) 7764–7768, https://doi.org/10.1002/anie.201702099.

[69] L. Lai, J.R. Potts, D. Zhan, L. Wang, C.K. Poh, C. Tang, H. Gong, Z. Shen, J. Lin, R. S. Ruoff, Exploration of the Active Center Structure of Nitrogen-Doped Graphene-Based Catalysts for Oxygen Reduction Reaction, Energy Environ. Sci. 5 (7) (2012) 7936–7942, https://doi.org/10.1039/C2EE21802J.

[70] D. Deng, X. Pan, L. Yu, Y. Cui, Y. Jiang, J. Qi, W.-X. Li, Q. Fu, X. Ma, Q. Xue, G. Sun, X. Bao, Toward N-Doped Graphene Via Solvothermal Synthesis, Chem. Mater. 23 (5) (2011) 1188–1193, https://doi.org/10.1021/cm102666r.

[71] K.N. Wood, K.X. Steirer, S.E. Hafner, C. Ban, S. Santhanagopalan, S.-H. Lee, G. Teeter, Operando X-Ray Photoelectron Spectroscopy of Solid Electrolyte Interphase Formation and Evolution in Li_2S-P_2S_5 Solid-State Electrolytes, Nat. Commun. 9 (1) (2018) 2490, https://doi.org/10.1038/s41467-018-04762-z.

[72] G. Nazri, Preparation, Structure and Ionic Conductivity of Lithium Phosphide, Solid State Ionics 34 (1) (1989) 97–102, https://doi.org/10.1016/0167-2738(89)90438-4.
[73] N. Wu, Y. Li, A. Dolocan, W. Li, H. Xu, B. Xu, N.S. Grundish, Z. Cui, H. Jin, J. B. Goodenough, In Situ Formation of Li_3P Layer Enables Fast Li^+ Conduction across Li/Solid Polymer Electrolyte Interface, Adv. Funct. Mater. 30 (22) (2020) 2000831, https://doi.org/10.1002/adfm.202000831.
[74] W. Xu, J.L. Wang, F. Ding, X.L. Chen, E. Nasybutin, Y.H. Zhang, J.G. Zhang, Lithium Metal Anodes for Rechargeable Batteries, Energy Environ. Sci. 7 (2) (2014) 513–537, https://doi.org/10.1039/c3ee40795k.
[75] J.T. Vaughey, G. Liu, J.-G. Zhang, Stabilizing the Surface of Lithium Metal, MRS Bull. 39 (5) (2014) 429–435, https://doi.org/10.1557/mrs.2014.88.
[76] G.X. Li, Q.Q. Huang, X. He, Y. Gao, D.W. Wang, S.H. Kim, D.H. Wang, Self-Formed Hybrid Interphase Layer on Lithium Metal for High-Performance Lithium-Sulfur Batteries, ACS Nano 12 (2) (2018) 1500–1507, https://doi.org/10.1021/acsnano.7b08035.
[77] L.P. Hou, X.Q. Zhang, B.Q. Li, Q. Zhang, Challenges and Promises of Lithium Metal Anode by Soluble Polysulfides in Practical Lithium-Sulfur Batteries, Mater. Today 45 (2021) 62–76, https://doi.org/10.1016/j.mattod.2020.10.021.
[78] Y. Zhao, Y. Ye, F. Wu, Y. Li, L.i. Li, R. Chen, Anode Interface Engineering and Architecture Design for High-Performance Lithium-Sulfur Batteries, Adv. Mater. 31 (12) (2019) 1806532, https://doi.org/10.1002/adma.201806532.
[79] H. Shi, X. Ren, J. Lu, C. Dong, J. Liu, Q. Yang, J. Chen, Z.-S. Wu, Dual-Functional Atomic Zinc Decorated Hollow Carbon Nanoreactors for Kinetically Accelerated Polysulfides Conversion and Dendrite Free Lithium Sulfur Batteries, Adv. Energy Mater. 10 (39) (2020) 2002271, https://doi.org/10.1002/aenm.202002271.
[80] X. Zhu, Y. Li, R. Li, K. Tu, J. Li, Z. Xie, J. Lei, D. Liu, D. Qu, Self-Assembled N-Doped Carbon with a Tube-in-Tube Nanostructure for Lithium-Sulfur Batteries, J. Colloid Interface Sci. 559 (2020) 244–253, https://doi.org/10.1016/j.jcis.2019.10.027.
[81] Y. Cui, X. Zhao, R. Guo, Improved Electrochemical Performance of $La_{0.7}Sr_{0.3}MnO_3$ and Carbon Co-Coated $LiFePO_4$ Synthesized by Freeze-Drying Process, Electrochim. Acta 55 (3) (2010) 922–926, https://doi.org/10.1016/j.electacta.2009.08.020.